ACS Catalysis

Subscriber access provided by Northern Illinois University

Article

High Performance Au-Pd Supported on 3D Hybrid Strontium-Substituted Lanthanum Manganite Perovskite Catalyst for Methane Combustion

Yuan Wang, Hamidreza Arandiyan, Jason Anthony Scott, Mandana Akia,
Hongxing Dai, Jiguang Deng, Kondo-Francois Aguey-Zinsou, and Rose Amal

ACS Catal., **Just Accepted Manuscript** • DOI: 10.1021/acscatal.6b01685 • Publication Date (Web): 06 Sep 2016

Downloaded from http://pubs.acs.org on September 11, 2016

Just Accepted

“Just Accepted” manuscripts have been peer-reviewed and accepted for publication. They are posted online prior to technical editing, formatting for publication and author proofing. The American Chemical Society provides “Just Accepted” as a free service to the research community to expedite the dissemination of scientific material as soon as possible after acceptance. “Just Accepted” manuscripts appear in full in PDF format accompanied by an HTML abstract. “Just Accepted” manuscripts have been fully peer reviewed, but should not be considered the official version of record. They are accessible to all readers and citable by the Digital Object Identifier (DOI®). “Just Accepted” is an optional service offered to authors. Therefore, the “Just Accepted” Web site may not include all articles that will be published in the journal. After a manuscript is technically edited and formatted, it will be removed from the “Just Accepted” Web site and published as an ASAP article. Note that technical editing may introduce minor changes to the manuscript text and/or graphics which could affect content, and all legal disclaimers and ethical guidelines that apply to the journal pertain. ACS cannot be held responsible for errors or consequences arising from the use of information contained in these “Just Accepted” manuscripts.

ACS Publications

ACS Catalysis is published by the American Chemical Society. 1155 Sixteenth Street N.W., Washington, DC 20036

Published by American Chemical Society. Copyright © American Chemical Society. However, no copyright claim is made to original U.S. Government works, or works produced by employees of any Commonwealth realm Crown government in the course of their duties.

High Performance Au–Pd Supported on 3D Hybrid Strontium-Substituted Lanthanum Manganite Perovskite Catalyst for Methane Combustion

Yuan Wang,† Hamidreza Arandiyan,†* Jason Scott,†* Mandana Akia,‡ Hongxing Dai,§* Jiguang Deng,§ Kondo-Francois Aguey-Zinsou⊥ and Rose Amal†

Yuan Wang, Dr. Hamidreza Arandiyan, Dr. Jason Scott, Prof. Rose Amal
†Particles and Catalysis Research Group, School of Chemical Engineering, The University of New South Wales, Sydney, NSW 2052, Australia

Prof. Kondo-Francois Aguey-Zinsou
⊥MERLin Group, School of Chemical Engineering, The University of New South Wales, Sydney, NSW 2052, Australia

Dr. Mandana Akia
‡Mechanical Engineering Department, University of Texas-Rio Grande Valley, 1201 West University Drive, Edinburg, TX 78539, USA.

Prof. Hongxing Dai, Dr. Jiguang Deng,
§Beijing Key Laboratory for Green Catalysis and Separation, and Laboratory of Catalysis Chemistry and Nanoscience, Beijing University of Technology, Beijing 100124, China

ABSTRACT: Bimetallic Au–Pd alloy nanoparticles (NPs) dispersed on nanohybrid three-dimensionally ordered macroporous (3DOM) $La_{0.6}Sr_{0.4}MnO_3$ (LSMO) perovskite catalysts were fabricated via the L-lysine-mediated colloidal crystal-templating and reduction routes. The obtained AuPd/3DOM LSMO samples possess a nanovoid-like 3DOM construction with well-dispersed Au–Pd alloy NPs (2.05–2.35 nm in size) on the internal walls of the macropores. The Au-Pd alloy presence favored catalytic activity for methane combustion. The 3DOM LSMO support exhibits three key attributes: (i) a large surface area (32.0–33.8 m^2/g) which aids high dispersion of the noble metal NPs on the support surface; (ii) abundant Brønsted acid sites which facilitate reactant adsorption and activation; and (iii) thermal stability. The AuPd/3DOM LSMO has been synthesized with the beneficial properties, including a richness of adsorbed oxygen species, increased oxidized noble metal species, low-temperature reducibility, and strong noble metal–3DOM LSMO interaction, all contributing to provide enhanced activity and a structure with high thermal and hydrothermal stability. *In-situ* diffuse reflectance infrared Fourier transform spectroscopy studies revealed that including Au in the bimetallic system accelerated the reaction rate and altered the reaction pathway for methane oxidation by enriching the adsorbed oxygen species and decreasing the bonding strength between the reaction intermediates and the Pd atoms.

KEYWORDS: strontium-substituted lanthanum manganite; bimetallic gold-palladium catalyst; three-dimensionally ordered macroporous perovskite; methane combustion; synergism.

1. INTRODUCTION

There is a great interest in using methane as an alternative to coal and oil, given its low carbon emissions.[1] However, due to incomplete combustion, un-burnt methane always exists in the exhaust. Methane removal is needed because of its strong greenhouse effect with a global warming potential 23 times higher than that of CO_2.[2-4] Catalytic combustion of methane is regarded as an efficient way to conventional thermal combustion for energy production.[5] The temperature of exhaust gases from natural gas vehicles (NGVs) [6] is relatively low (typically varying between 300 and 500 °C), therefore the abatement of methane emissions in the NGV exhaust requires catalysts that combine high activity with great resistance to thermal coarsening so as to maintain high combustion rates.[5] Au as a catalyst has drawn little attention due to its sluggish nature and low melting point (1063 °C). Nevertheless, since Hutchings et al. [7] first reported in 1985 that some Au catalysts were active for the hydrochlorination of acetylene, Au catalysts have gained increasing attention due to their unique physicochemical properties, and numerous reactions can be catalyzed by Au catalysts with high performance. Recently, it has been shown that Pt or Pd alloyed with Au displayed high catalytic activities for H_2O_2 synthesis, N_2O decomposition, toluene oxidation as well as methane combustion.[8] For instance, Hutchings et al. [9] investigated the oxidation of toluene over Au–Pd/TiO_2 catalysts and found that the Au performed as an electron donor for Pd and the active catalyst had a Pd-enriched surface where the surface-bound oxygen-centered radicals played a crucial role in toluene activation. Chen et al. [5] reviewed a study on the catalytic oxidation of CH_4, and pointed out that the addition of Au to Pd can boost the overall activity, stability, and selectivity of the supported Pd catalysts. Chen and co-workers [10] investigated the mechanism of the promotional effect of Pd–Au alloy catalyst for the synthesis of vinyl acetate and found that the main role of Au in the bimetallic system was to isolate Pd atoms which facilitated the desirable coupling of critical surface species and hindered the formation of unfavorable reaction by-products. Additionally, many efforts have been made to study the physical properties of perovskite-type oxides (ABO_3) which exhibit promising catalytic activity. Levasseur et al.[11] synthesized a series of $LaBO_3$ (B = Co, Fe, and Mn) catalysts by applying a strategy called “reactive grinding” and found that the catalytic activity for methanol oxidation followed the order of $LaMnO_3 > LaCoO_3 > LaFeO_3$. Due to its outstanding low-temperature reducibility and large number of oxygen vacancies, the perovskite-type oxide (e.g., $LaMnO_3$) exhibited better catalytic performance than TiO_2 and Co_3O_4 for the low-temperature oxidation of volatile organic compounds (VOCs).[9] Considering the advantages of noble metals (Au and Pd) and ABO_3, a catalyst system coupling noble metals and ABO_3 is anticipated to deliver good catalytic activity for methane combustion.

Three-dimensionally ordered macroporous (3DOM) materials have been previously employed to catalyze the oxidation of VOCs [12-14] due to their good transportation and diffusion properties induced by their interconnected pore network. Using differently sized polymethyl methacrylate (PMMA) microspheres as a template and metal nitrates as the precursor, Arandiyan et al.[15] synthesized 3DOM-structured $La_{1-x}Ce_xCoO_3$ ($0 > x > 0.9$) with a mesopore diameter of 10 nm and surface areas of 16.5–35.4 m^2/g, where the 3D highly ordered macro/mesoporous $La_{0.7}Ce_{0.3}CoO_3$ sample exhibited high catalytic activity ($T_{90\%}$ = 555 °C) for CH_4 oxidation. Earlier, Dai’s research group adopted the PMMA-templating and polyvinyl alcohol (PVA)- or polyvinyl pyrrolidone (PVP)-assisted reduction approaches to successfully generate a range of 3DOM material-supported Au NPs, for example, Au/3DOM Mn_2O_3 (surface area = 34–38 m^2/g) [16], Au/3DOM $La_{0.6}Sr_{0.4}MnO_3$ (surface area = 31–32 m^2/g) [17], Au/3DOM $LaCoO_3$ (surface area = 24–29 m^2/g) [18], and Au/3DOM Co_3O_4 (surface area = 33–36 m^2/g) [19]. Compared to the bulk material-supported Au catalysts, the 3DOM-structured counterparts exhibited better catalytic activity for oxidizing VOCs and/or CO.[16-19] Nevertheless, one weakness of these noble metal-loaded porous catalysts is their poor hydrothermal stability.

For the first time, 3DOM $La_{0.6}Sr_{0.4}MnO_3$ with 1–3 wt% Au–Pd alloy NPs dispersed on the interconnected skeletons was prepared and the reaction mechanism of methane oxidation was studied by *in-situ* DRIFTS over the obtained bimetallic catalysts. The research demonstrates that 3AuPd/3DOM LSMO exhibits a low complete methane conversion temperature (350 °C) and high thermal and hydrothermal stability. Catalyst characterization confirms the formation of bimetallic sites and shows that the structures and chemical states remain almost unchanged during reaction at 350 °C and in the presence of 1–5 vol% water vapor. The blending of surface chemistry (rich adsorbed oxygen, activated noble metal species, acidic sites), structure (distinct 3DOM architecture and high surface area), and strong electronic interaction between the Au and Pd as well as the noble metal alloy with the 3DOM support contributes to the promotion of catalytic activity and stability for methane combustion. In addition, the nature of the key reaction intermediates, mechanism and active ensembles are examined by *in-situ* DRIFTS under simulated reaction conditions for methane oxidation. By understanding the reaction mechanism of methane oxidation and the manner by which bimetallic catalysts assist in the reaction, we can pave a new synthetic route to design hybrid bimetallic catalysts.

2. EXPERIMENTAL

2.1 Synthesis of 3DOM LSMO and Au–Pd supported catalysts

Well-arrayed colloidal crystal template PMMA microspheres with an average diameter of ca. 218 nm (estimated according to the SEM images (Figure S1A) and supported by particle size distribution analysis (Zetasizer Nano Z, Figure S1B) were synthesized according to a procedure described elsewhere [20]. The zAu$_1$Pd$_2$/3DOM LSMO (z = 1, 2, and 3 wt%) catalysts were prepared by a L-lysine-assisted PMMA microsphere hard-templating method with $La(NO_3)_3 \cdot 6H_2O$, $Sr(NO_3)_2$, and $Mn(NO_3)_2$ as the metal precursors. The Au–Pd NPs were loaded on the surface of the perovskite support using an N_2-bubbled reduction method, involving the reduction of $HAuCl_4$ and $NaPdCl_4$

solutions under an N_2 atmosphere with methanol, ethylene glycol (EG), and PVA as the capping agent (Scheme 1 and Figure S2). The typical procedures for synthesizing $1Au_xPd_y$/1DDN LSMO (Au/Pd molar ratio ($x : y$) = 1 : 1, 1 : 2, and 1 : 3) and $z Au_1Pd_2$/3DOM LSMO catalysts (z = 1, 2, and 3 wt%) are described in the Supporting Information.

2.2 Catalyst characterization and activity measurements

Each of the as-obtained samples was characterized by X–ray diffraction (XRD) spectroscopy, high-resolution scanning electron microscopy (HRSEM), energy dispersive spectroscopy (EDS), high-resolution transmission electron microscopy (HRTEM), high-angle annular dark-field scanning transmission electron microscopy and energy-dispersive X-ray spectroscopy (HAADF–STEM–EDS), N_2 physisorption (Brunauer–Emmett–Teller, BET), 3D environmental atomic force microscope (3D–eAFM), inductively coupled plasma atomic emission spectroscopy (ICP–AES), H_2 temperature-programmed reduction (H_2-TPR), NH_3 temperature-programmed desorption (NH_3-TPD), X-ray photoelectron spectroscopy (XPS) and *in-situ* diffuse reflectance infrared Fourier transform spectroscopy (*in-situ* DRIFTS). Details on the characterization procedures can be found in Supporting Information. Methane oxidation over the obtained catalysts was conducted according to the process described in Supporting Information (Figure S3)

3. RESULTS AND DISCUSSION

3.1 Crystal structure and textural properties of 3DOM LSMO and Au–Pd NPs

XRD patterns of the 3DOM LSMO support (Figure S4) confirm formation of the cubic ABO_3 phase which is in good agreement with the standard $La_{0.6}Sr_{0.4}MnO_3$ sample (JCPDS PDF No. 04-016-6114)[13]. The calcination conditions are appropriate for generating single-phase $ABO_{3,}$ as illustrated by the XRD results of 3DOM LSMO with well-defined crystallinity. In the case of the supported Au, Pd, and bimetallic Au–Pd catalysts, loading the noble metal NPs does not alter the ABO_3 structure. The average crystallite sizes ($D_{support}$) of the zAu$_1$Pd$_2$/3DOM LSMO samples were estimated using the Scherrer equation, as summarized in Table 1. The average crystallite size of 3DOM LSMO is ca. 32.9 nm, which is close to those (32.0–33.8 nm) of the zAu$_1$Pd$_2$/3DOM LSMO samples. No significant diffraction signals assignable to Au and/or Pd are observed, possibly due to the low Au and Pd loadings (1–3 wt%) and high dispersion of Au and Pd NPs on the 3DOM LSMO surface.[17] The actual loadings of Au and Pd on the 3DOM LSMO-supported noble metal samples are summarized in Table 1. It is found that the actual Au and Pd loadings are slightly lower than their nominal values, indicating that most of the Au and Pd is deposited on the 3DOM LSMO support. The small difference between the nominal and actual loadings indicates that the N_2 gas-bubble-assisted reduction strategy is a feasible approach for synthesizing supported Au–Pd catalysts.

Typical N_2 adsorption–desorption isotherms and pore size distributions of the 3DOM LSMO and zAu$_1$Pd$_2$/3DOM LSMO samples are shown in Figure S5. The N_2 isotherm observed for each sample is classified as a type II isotherm, indicating the formation of a 3DOM structure (Figure S5(A)). The low-pressure portion of the almost linear middle section of the isotherm, which is attributed to multilayer adsorption, suggests that the sample is macroporous. A H3-type hysteresis loop is observed in the high relative pressure (p/p_0) range of 0.9–1.0, which is associated with capillary condensation taking place in the mesopores, and confirms the presence of mesopores within the wall structure.[21] Figure S5(B) illustrates the BJH pore size distributions of the samples, each of which includes two obvious peaks: one sharp peak at around 3–5 nm and one broad peak in the range of 40–100 nm. The results indicate the co-existence of macropores and textural mesopores within the skeletons of zAu$_1$Pd$_2$/3DOM LSMO, which is verified by the HRSEM and HRTEM analyses (see below) and pore size distributions (2.05–2.35 nm). The BET surface areas and pore volumes of the zAu$_1$Pd$_2$/3DOM LSMO samples are in the ranges of 32.0–33.8 m^2/g and 0.106–0.130 cm^3/g, respectively (Table 1), which are close to those (32.4 m^2/g and 0.123 cm^3/g) of the 3DOM LSMO support and much higher than those (4.32 m^2/g and 0.017 cm^3/g) of the 1AuPd/1DDN LSMO sample. The 3AuPd/3DOM LSMO sample possesses a large BET surface area (33.8 m^2/g) due to its thinner walls and nanovoid generation. Hence, in contrast to the 1AuPd/1DDN LSMO sample, the zAu$_1$Pd$_2$/3DOM LSMO samples containing mesopores within a macroporous skeleton possess higher surface areas that can provide more active sites, with the highly developed pore structure also facilitating diffusion and adsorption of the reactant molecules.[14] Such unique properties are anticipated to be beneficial for promoting the catalytic activity of the sample.

3.2 HRSEM and HAADF–STEM

Figures 1 and 2 show the HRSEM and HRTEM images of 3DOM LSMO, single Au, Pd and bimetallic Au-Pd on 3DOM LSMO samples as well as the 3D–eAFM image of the PMMA template. As shown in Figures 1a and 1b, the HRSEM and 3D–eAFM reconstruction displays a hexagonal array of well-calibrated circular microspheres. The one-dimensionally disordered nonporous 1AuPd/1DDN LSMO sample shows an irregular morphology with a particle size range of 200–600 nm (Figure 1c). The formation of monolithic nanohybrid ABO_3 with a 3D hierarchical porosity in the 3DOM LSMO support (Figure 1d–f) is observed, exhibiting a pore diameter of about 140 nm. The average pore diameter of the noble metal supported 3DOM LSMO samples (Figure 1g–l) is smaller by 10–35 %, when compared with the initial microsphere size of the PMMA template (pore size = 218 nm) as shown in Figure S6. The shrinkage is caused by the melting of the PMMA template and the sintering of the produced ABO_3. Introducing organics, including L-lysine (1.00 g), methanol (3.0 mL), and EG (3.0 mL) improves the quality of the AuPd/3DOM LSMO pore structure (Figures S7 and S8). Upon adding PVA, high-quality 3DOM architectures with interconnected pore channels were generated in all of the 3DOM LSMO samples under different fabrication conditions (Figure 1f, h, j and l). From the

HRTEM images, it is clear that a large number of noble metal NPs are highly dispersed on the surface of the 3DOM LSMO framework with a mean NP size of 2.05–2.35 nm (Figure 2). Additionally, the intraplanar spacing (*d* value) of the obtained 3DOM LSMO samples was found to be 0.260–0.262 nm, in good agreement with that of the (110) crystal plane of the standard $La_{0.6}Sr_{0.4}MnO_3$ sample (0.263 nm, JCPDS PDF No. 04–016–6114). To examine the morphology and composition of the Au–Pd NPs, the HAADF–STEM–EDS technique was used to map the distribution of Au, Pd, and other elements in the 1AuPd/3DOM LSMO sample, as shown in Figures 3 and S9. The EDS phase maps and line profiles of the as-obtained Pd and Au NPs show a homogeneous distribution of the two elements over the entire particle (Figure 3a–c). Furthermore, the 3D visualization of Pd and Au as well as the EDS intensity line profiles of the 1AuPd/3DOM LSMO sample eliminates any structural variations such as core-shell and/or separate phases with the Au–Pd alloy NPs being highly dispersed on the surface of the 3DOM LSMO skeleton structure (Figure 3d–f). An estimation of Au–Pd alloy NP sizes from the HRTEM images (Figures S10–12) indicates that the mean NP sizes in AuPd/3DOM LSMO (2.05-2.20 nm) are uniform and slightly smaller than those for 1Au/3DOM LSMO (2.3 nm) and 1Pd/3DOM LSMO (2.2 nm). The noble metal NPs seen in the high magnification TEM images (Figures S10b, 11b, and 12b) imply there is a strong interfacial interaction with 3DOM LSMO as seen by the partial incorporation of oxidized NP species into the bulk structure of the 3DOM LSMO support (i.e. a strong metal–support interaction (SMSI) effect is present).[22] The interaction between the Au–Pd NPs and 3DOM LSMO might be conducive to lattice oxygen mobility and making it favorable for producing oxygen vacancies on the AuPd/3DOM LSMO surface as will be discussed in more detail in the XPS section.

3.3 Surface elemental composition, metal oxidation state, and adsorbed oxygen

Profiles of the Mn 2p, Au 4f, and Pd 3d regions of the XPS spectra are provided in Figure 4 with key data extracted from the profiles given in Table S1. For each sample, there is an asymmetrical Mn $2p_{3/2}$ XPS signal that can be deconvoluted into three components at binding energy (BE) values = 641.2, 642.4, and 643.8 eV (Figure 4A), assignable to surface Mn^{3+}, Mn^{4+}, and satellite species,[13] respectively. The surface Mn^{4+}/Mn^{3+} molar ratio of the 1AuPd/1DDN LSMO sample (1.26) is lower than that of the 3DOM LSMO sample (1.42). On introducing noble metal NPs, however, the $z$$Au_1Pd_2$/3DOM LSMO surface Mn^{4+}/Mn^{3+} molar ratio decreases (1.15–0.89), prompting the Pd^{2+}/Pd^0 and $Au^{\delta+}/Au^0$ molar ratios to rise (0.31–0.41 and 0.73–1.23, respectively). The 3AuPd/3DOM LSMO sample possesses the lowest surface Mn^{4+}/Mn^{3+} molar ratio (0.89) and the highest Pd^{2+}/Pd^0 (1.23) and $Au^{\delta+}/Au^0$ (0.42) molar ratios. The XPS results reveal that depositing the Au and Pd elevates the Mn^{3+} content, implying there is a strong interaction between the Au-Pd NPs and LSMO. That is, the LSMO support partially oxidises the Au/Pd deposits (undergoing partial reduction as a result) as described by the following Eqns. ((1) and (2)):

$$\mathrm{Au}^0 + \mathrm{Mn}^{4+} \rightarrow \mathrm{Au}^{\delta+} + \mathrm{Mn}^{3+} \qquad (1)$$

$$\mathrm{Pd}^0 + \mathrm{Mn}^{4+} \rightarrow \mathrm{Pd}^{\delta+} + \mathrm{Mn}^{3+} \qquad (2)$$

The extent to which partial oxidation occurs increases with increasing Au/Pd loading (Table S1) which has an impact on catalyst performance as is discussed later. The Pd 3d and Au 4f XPS spectra of the $z$$Au_1Pd_2$/3DOM LSMO samples provide strong evidence to support this hypothesis.

The Au 4f spectra of the samples can be deconvoluted into four components (Figure 4B) with the two peaks at BE = 83.8 and 87.5 eV representing the surface Au^0 species and the two peaks at BE = 84.7 and 88.6 eV due to the surface $Au^{\delta+}$ species. It is apparent that the $Au^{\delta+}/Au^0$ molar ratio increases on adding Pd (Table S1). The $Au^{\delta+}/Au^0$ molar ratios of the supported Au–Pd alloy catalysts (0.31–0.42) are higher than that of the supported Au catalyst (0.20) and increase with the loading of Au–Pd alloy NPs from 1 to 3 wt%. It has been stated by others that a higher $Au^{\delta+}/Au^0$ molar ratio is indicative of a better ability to activate oxygen molecules.[22] Similar phenomena are observed in the Pd 3d XPS spectra (Figure 4C), in which the Pd^{2+}/Pd^0 molar ratios of the AuPd/3DOM LSMO catalysts increase as compared with the Pd/3DOM LSMO catalyst. The asymmetrical Pd 3d XPS spectrum of each sample can be deconvoluted into four components: the two peaks at BE = 335.4 and 340.8 eV are assigned to the surface Pd^0 species, while the two peaks at BE = 337.0 and 342.2 eV are attributed to the surface Pd^{2+} species.[23] The 1AuPd/3DOM LSMO sample exhibits a Pd^{2+}/Pd^0 molar ratio (0.73) which is slightly higher than that of the 1Pd/3DOM LSMO sample (0.71) and considerably higher than that of 1AuPd/1DDN LSMO (0.50), suggesting that Au addition can enhance the Pd^{2+} concentration on the surface [23-24]. The result is in good agreement with Hutchings's finding that Au could act as an electron promoter for Pd in bimetallic Au–Pd NPs on TiO_2.[25] Additionally, it is observed that the Au 4f and Pd 3d XPS peaks of the 1AuPd/3DOM LSMO and 2AuPd/3DOM LSMO samples shift to lower and higher BEs (by ca. 0.3 and 0.5 eV), respectively, in relation to the 1Au/3DOM LSMO and 1Pd/3DOM LSMO catalysts (Figure S13). Such a BE shift has been previously reported and reflects an electronic structure modification to the surface Au and Pd atoms. That is, electron transfer from the Pd to Au generating more oxidized Pd while simultaneously Au and Pd donate electrons to the LSMO support oxidizing Au and further oxidizing Pd, an effect evidenced by the decrease in Mn^{4+}/Mn^{3+} ratio.[26] From Figure 4D, a broad and asymmetrical O 1s XPS spectrum for each sample can be deconvoluted into three components at BE = 529.5, 531.2, 532.2 and 533.4 eV, ascribable to the surface lattice oxygen (O_{latt}), adsorbed oxygen (O_{ads}), hydroxyl and/or carbonate species, and adsorbed molecular water species, respectively.[27] The electrophilic species (O_{ads}, e.g., O_2^-, O_2^{2-} or O^-) can play a vital role in the deep oxidation of organics.[28] From Table S1, the surface O_{ads}/O_{latt} molar ratio follows the order: 3AuPd/3DOM LSMO (0.94) > 2AuPd/3DOM LSMO (0.64) > 1AuPd/3DOM LSMO (0.55) > 1Pd/3DOM LSMO (0.49) > 1AuPd/1DDN LSMO (0.44) > 1Au/3DOM LSMO (0.43) > 3DOM

LSMO (0.34). The higher O_{ads}/O_{latt} molar ratio for the Au-Pd alloy catalysts suggests that the bimetallic system has a strong capacity to activate oxygen, potentially boosting its performance for CH_4 combustion. Burch et al. [29] reported that the Pd^{2+} and O^{2-} species at the surface of PdO could readily activate the almost non-polar C–H bonds by a heterolytic mechanism. Hence, the actual surface composition of the noble metals (Pd^0, Au^0 or $Pd^{\delta+}$, $Au^{\delta+}$) is crucial in determining the inherent activity of the catalyst.

3.4 Reducibility and surface acidity

H_2-TPR analysis was conducted to assess the redox properties of the as-obtained samples (Figure 5A). Since La^{3+} and Sr^{2+} are non-reducible under the H_2-TPR conditions, the peaks observed in the LSMO sample can be attributed to the reduction of Mn^{n+} species.[13] The two peaks, namely α (at ~310 °C) and β (at ~650 °C), are credited to the reduction of Mn^{4+} to Mn^{3+} (Eqn (3)) and Mn^{3+} to Mn^{2+} [12, 30] (Eqn (4)), respectively, with a shoulder at 380 °C due to the single-electron reduction of Mn^{3+} located in a co-ordinatively-unsaturated microenvironment (Eqn (5)).[30]

$$\mathrm{La_{1-x}Sr_xMn^{III}_{1-x}Mn^{IV}_xO_3} + \frac{1}{2}x\mathrm{H_2} \rightarrow \mathrm{La_{1-x}Sr_xMn^{III}O_{3-x/2}} + \frac{1}{2}x\mathrm{H_2O} \qquad (3)$$

$$\mathrm{La_{1-x}Sr_xMnO_{3-x/2}} + \frac{1}{2}\mathrm{H_2} \rightarrow \frac{1}{2}(1-x)\mathrm{La_2O_3} + \mathrm{MnO} + x\mathrm{SrO} + \frac{1}{2}\mathrm{H_2O} \qquad (4)$$

$$\mathrm{La_{1-x}Sr_xMn^{III}_{1-x}Mn^{IV}_{x+\delta/2}O_{3+\delta}} + \delta\mathrm{H_2} \rightarrow \mathrm{La_{1-x}Sr_xMn^{III}_{1-x}Mn^{IV}_xO_3} + \delta\mathrm{H_2O} \qquad (5)$$

When Au, Pd or Au–Pd NPs are loaded on the surface of 3DOM LSMO, the reduction peaks shift to lower temperatures, indicating that the noble metal NPs facilitate reducibility of the sample. Improving the low-temperature reducibility is beneficial for catalytic performance.[12-14, 20]

In the case of the monometallic Au and Pd catalysts, the α peak moved significantly (to 160 °C) for the 1Pd/3DOM LSMO whereas it moved slightly (to 305 °C) for the 1Au/3DOM LSMO, suggesting that the PdO_x species are more readily reducible than the AuO_x species. The reduction temperatures (200 and 162 °C) of the α peaks of the bimetallic catalysts are between those of the Au and Pd catalysts and lower than that of the supported Pd sample when the loading was 3 wt% (125 °C), implying the Au–Pd catalyst is in an alloyed state and strongly interacts with the 3DOM LSMO support, rather than existing as a physical mixture of the Au and Pd catalysts.

Variations in the surface acidity/basicity between 3DOM LSMO and 1DDN LSMO were identified using NH_3-TPD analysis. Two peaks are observed in the NH_3-TPD profile for 3DOM LSMO (Figure 5B), which leads to the presumption that weak acidic sites (665 °C) and Brønsted acidic sites (860 °C), exist on the surface, in good agreement with the results described by Lu and co-workers.[31] In contrast, the 1DDN LSMO sample shows one small weak acidic site peak at a temperature of 680 °C. Brønsted acidic sites have been reported to invoke catalytic enhancement with supported Pd and Pt NPs, helping to adsorb and activate reactant molecules during the catalytic process.[32]

3.5 Catalytic performance

Figure 6 depicts the catalytic performance of the AuPd/3DOM LSMO samples for CH_4 combustion. It is apparent from Figure 6A that Au or Pd alone only gives a mildly enhanced activity, whereas alloying the Au and Pd invokes a substantial improvement in catalytic performance, illustrating a clear synergism between the two metals. With the rise in overall bimetallic metal loading to 3 wt% the activity also increases. The synergism between the Au–Pd alloy is further demonstrated on comparison with a physical mixture of the neat 1Au/3DOM LSMO and 1Pd/3DOM LSMO (same overall metal loading, Figure S14(A)). Comparing the catalytic performance of the samples on the basis of $T_{10\%}$, $T_{50\%}$, and $T_{90\%}$ (Table S1, the temperatures at which CH_4 conversion are 10, 50, and 90 %, respectively), it is apparent that the activity of the bimetallic Au–Pd catalysts increases with increasing loading. The 1AuPd/3DOM LSMO gives $T_{10\%}$, $T_{50\%}$, and $T_{90\%}$ values of 304, 350, and 382 °C which are lower than the 1AuPd/1DDN LSMO sample and considerably lower than the neat 3DOM LSMO sample (Figure S14(B)). Figure 6A illustrates the relationship between catalytic activity and molar ratios of the surface species (i.e. O_{ads}/O_{latt}, Pd^{2+}/Pd^0, and $Au^{\delta+}/Au^0$). The comparison reveals that each of these attributes has a clear influence on catalytic performance.[7] Appraisal of the zAu$_1$Pd$_2$/3DOMLSMO catalysts on the basis of turnover frequencies (TOFs) and the reaction rate at 270 °C is provided in Table 2. The $TOF_{Au–Pd}$ of the samples decrease in the order of 3AuPd/3DOM LSMO > 2AuPd/3DOM LSMO > 1AuPd/3DOM LSMO > 1Pd/3DOM LSMO >1AuPd/1DDN LSMO > 1Au/3DOM LSMO.

Figure 6B illustrates the change in TOF with the amount of H_2 consumed during H_2-TPR analysis for the neat and bimetallic catalyst compositions and loadings. The change in TOF with deposit make-up (mono- and bimetallic) and bimetallic loading indicates the perovskite support is having an impact on the catalyst activity associated with the bimetallic deposits. That is, the catalytic performance is not solely governed by the additional active sites introduced by the greater number of Au/Pd atoms on the surface. The roughly linear relationship between the TOF and the reducibility of the perovskite support (i.e. H_2 consumed during the H_2-TPR) as the bimetallic loading increases implies an effect of the support is responsible for embellishing the activity of the Au/Pd deposits. A potential explanation for the contribution of the support in enhancing the Au/Pd activity can be found in the XPS results (Table S1), in particular the decreasing Mn^{4+}/Mn^{3+} ratio (reflecting a partial reduction in the support) and increasing Pd^{2+}/Pd^0 and $Au^{\delta+}/Au^0$ (reflecting a partial oxidation of the deposits) with increasing bimetallic loading. The support acts to withdraw electrons from the bimetallic deposits, which amplifies their activity beyond just the simple catalyst loading effect. The result ties in with the findings from Figure S15B which show pre-treating the catalyst in oxygen is beneficial for activity.

It is interesting also to note that earlier work[12] indicated an increased presence of Mn^{4+} on the neat LSMO perovskite correspondingly promoted its catalytic activity for methane oxidation. Here, the effect is opposite with there being an increase in activity as the Mn^{4+} presence decreases (Table S1). The contradictory effect can be explained on the basis of the catalytic activity is being dominated by the bimetallic deposits (and the concerted oxidising effect of the support) which supercedes any loss in active sites and activity by the associated reduction of Mn^{4+} in the perovskite support.

To assess the impacts of the Au/Pd molar ratio and catalyst pretreatment on performance, a range of $1Au_xPd_y$/1DDN LSMO (x/y = 1 : 1, 1 : 2, and 1 : 3) samples were synthesized with the $1Au_1Pd_2$/1DDN LSMO sample being pretreated in O_2 or H_2 at 300 °C for 2 h prior to activity assessment. In Figure S15(A) the Pd-rich catalysts ($1Au_1Pd_2$/1DDN LSMO, $1Au_1Pd_3$/1DDN LSMO, and 1Pd/1DDN LSMO) exhibit higher low-temperature activity (below 400 °C), as compared with the Au-rich catalyst. On adding Pd, the catalytic activity significantly increases with the rise in Au/Pd molar ratio to 1:2, but further increasing the Au/Pd molar ratio results in a decrease in activity. Hence, the best Au/Pd molar ratio is 1:2 with the sample providing the highest $TOF_{Au\text{-}Pd}$ ($0.0102\ s^{-1}$) and the lowest apparent activation energy (E_a = 72.4 kJ/mol). There remains debate in the literature on the Pd oxidation state that is most active for CH_4 oxidation. For instance, Cullis et al. [33] found that Pd^0 showed better activity on a γ-Al_2O_3 support for CH_4 oxidation, whereas Burch et al. [34] and Farrauto et al. [35] pointed out that the Pd^0 species over 4 wt% PdO/Al_2O_3 were less active or completely inactive toward CH_4 oxidation. After studying the active sites on Pd/Al_2O_3 for CH_4 oxidation, Matamet et al. [36] reported that Pd^{2+} species were the active sites especially at temperatures below 676 °C, but above this temperature the reduced Pd could also catalyze the reaction. In the present study (Figure S15(B)), pretreating the $1Au_1Pd_2$/ 1DDN LSMO catalyst in an O_2 atmosphere considerably improves catalyst performance, as compared with its untreated counterpart or subsequent pretreatment in a H_2 atmosphere. In contrast, the activity is marginally better when the catalyst is pretreated in H_2. The result indicates that the oxidized noble metal ($Au^{\delta+}$ and Pd^{2+}) species appear to be more active than the metallic (Au^0 and Pd^0) species toward CH_4 oxidation. The performance of alternative catalysts for methane oxidation from the literature is summarized in Table S2. Although being influenced by variations in the individual reaction environments, our best-performing 3AuPd/3DOM LSMO catalyst exhibits an improved activity compared to the selected catalysts.

3.6 Catalyst stability and impact of water vapor

Evidence of good catalytic stability can be seen in Figure 6C for the 3AuPd/3DOM LSMO sample run for 50-h at 350 °C and a GHSV = 50,000 mL/(g h). As moisture is a component of feedstock and reaction products, it is important to assess its impact on catalytic performance, particularly in terms of catalyst stability. Figure 6D illustrates the influence of water vapor (1.0, 3.0 or 5.0 vol%) on performance of the 3AuPd/3DOM LSMO, 1Pd/3DOM LSMO, 1Au/3DOM LSMO, and LSMO samples when it is introduced into the feed stream at 380 °C for 1 h. Over the 3DOM LSMO and 3AuPd/3DOM LSMO samples, the loss in activity arising from 3 and 5 vol% water vapor presence is completely reversible when the water vapor is removed. Catalytic activity over the 3DOM LSMO and 3AuPd/3DOM LSMO samples is not significantly influenced by 1.0 vol% H_2O vapor. The temporary loss in activity in the presence of water may be due to the competitive adsorption of H_2O, CH_4, and O_2 on the 3DOM LSMO and zAu$_1$Pd$_2$/3DOM LSMO catalysts. At a higher temperature (550 °C, Figure S16), the adsorption of oxygen may be stronger than that of H_2O on the samples, which is in agreement with others.[37] In contrast to the neat support and bimetallic catalyst, introducing water to the feed stream imposes both temporary and permanent losses to the performance of the 1Pd/3DOM LSMO and 1Au/3DOM LSMO samples, with the degree increasing as the water content rises. Again, the temporary loss in activity may be attributable to the competitive adsorption; however, the activity is not completely recoverable after introducing the water, whereby a second deactivation process may be in effect. HRTEM images of the 1AuPd/3DOM LSMO, 1Au/3DOM LSMO, and 1Pd/3DOM LSMO samples after exposure to water vapor (Figures S10–12) explain the irreversible deactivation of the monometallic catalysts. The sizes of the noble metal NPs in the monometallic catalysts increase from 2.25–2.35 to 8.43–13.48 nm upon exposure to water, whereas that of the noble metal NPs in the bimetallic Au–Pd catalyst increase from 2.15 to 3.76 nm. It appears that the water vapor promotes sintering of the Au and Pd NPs with the ensuing loss in dispersion, leading to a permanent loss in activity.

3.7 In-situ reaction mechanism

To probe the mechanism of methane oxidation over the bimetallic catalysts and understand the role of Au in the bimetallic system, *in situ* DRIFTS experiments were conducted with the spectra for 1Pd/3DOM LSMO and 1AuPd/3DOM LSMO provided in Figure 7. The IR absorption bands of Pd/3DOM LSMO (Figure 7A) can be separated into three spectral zones. The first spectral zone displays the adsorption bands mainly corresponding to gaseous methane and CH_3^- species, giving a sharp peak assignable to the C–H antisymmetric stretching vibration in a free molecule at 3014 cm^{-1} associated with the deformation vibration of C–H bonds at 1300 cm^{-1}.[38-39] The absorption band centered at C–H 1450 cm^{-1} represents the asymmetric stretching in CH_3^-. The second spectral zone encompasses absorption bands at 2330 and 2360 cm^{-1} ascribable to the C=O stretching mode of gaseous carbon dioxide.[40] The third spectral zone accounts for other vibrations by different species. The peaks at 1060 and 1155 cm^{-1} are assigned to the oxygen-oxygen stretching frequency of chemisorbed oxygen species (O^-) on LSMO.[41-42] Intense peaks at 1250 and 1415 cm^{-1} belong to the $\omega(CH_2)$ in formaldehyde (H_2CO), while peaks associated with formate ($HCOO^-$) due to strong asymmetric stretching, υ_{as} (C–O), are at 1550 and 1690 cm^{-1} and the absorption peak at 1840 cm^{-1}

representing the υ (C=O) stretching vibration.[43-45] Similar DRIFTS spectra are observed for the 1AuPd/3DOM LSMO sample (Figure 7B), with the exception of variations to the intermediate species from the third spectral zone. Specifically, there is no ω (CH_2) in formate (at 1250 and 1415 cm^{-1}) whereas a bidentate carbonate species appears at 1170 cm^{-1}. Additionally, the oxygen species at 1130 cm^{-1} is adsorbed on Au according to the spectra of 1Au/3DOM LSMO in Figure S17. No CO is detected with increasing reaction temperature, indicating complete methane combustion over the 1Pd/3DOM LSMO and 1AuPd/3DOM LSMO catalysts. It is apparent that the intensity of the CH_4 absorption bands (at 3014 and 1300 cm^{-1}) decrease with the rise in reaction temperature, while the intensity of the CO_2 absorption bands (at 2330 and 2360 cm^{-1}) simultaneously increases. The rate-determining step for the catalytic combustion of methane is often considered to be cleavage of the first C–H bond.[46] According to the DRIFTS spectra, CH_3^- species at 1300 cm^{-1} emerge at 200 °C over 1AuPd/3DOM LSMO while CH_3^- species are formed over Pd/ 3DOM LSMO at 300 °C. Moreover, nearly all the methane (at 1300 and 3014 cm^{-1}) is converted into CO_2 (2330 and 2360 cm^{-1}) at 550 °C for 1AuPd/3DOM LSMO, indicating an enhanced low-temperature conversion ability on adding Au, as compared with 1Pd/3DOM LSMO.

Based on the provided DRIFTS spectra and literature,[40-41, 47-48] the methane oxidation mechanism over the 1Pd/3DOM LSMO and 1AuPd/3DOM LSMO catalysts can be summarized as two separate sequences of elementary steps. The mechanism proposed for the 1Pd/3DOM LSMO catalyst involves electron transfer from the PdO to LSMO, as was evidenced by XPS where the Mn^{4+}/Mn^{3+} ratio decreased in the catalyst. The O_2 is activated by electrons on the LSMO to form O^- species, with the resulting O^- sites activating C-H bonds in CH_4 promoting dehydrogenation into CH_3^- and OH^-. The CH_3^- and OH^- subsequently bond to unsaturated sites on the PdO and undergo further H-abstraction to form H^+ and H_2CO. The H^+ interacts with O^- to generate H_2O while H_2CO is oxidized first to form

$HCOO^-$ and then to generate CO_2 which completes a catalytic turnover. The mechanism coincides with other mechanistic assessments for Pd catalysts reported previously [49] which are based on kinetic and isotopic methods combined with density functional theory (DFT) calculations.

The presence of Au in the bimetallic 1AuPd/3DOM LSMO accelerated the reaction rate and altered several aspects of the reaction pathway (as shown in Scheme 2). According to XPS, the Au attracts electrons from the Pd making it more electronegative. Concurrently, electrons are also transferred from Au and Pd to the LSMO as evidenced by the additional decrease in the Mn^{4+}/Mn^{3+} ratio for the bimetallic system. Thus, O_2 can be activated by electrons from both the Au and LSMO surface to generate O^- species which can be verified by the oxygen species ratio from XPS (step i). When CH_4 is dehydrogenated to form CH_3^- and OH^- (step ii), the additional active oxygen species promote CH_3^- dissociation into $HCOO^-$ which is subsequently oxidized to give bidentate carbonate, bonded to Pd via two oxygens (step iv). CO_2 is then generated (step v) to complete the turnover cycle.

To further appreciate the role of Au in the bimetallic system, the ease of desorption of adsorbed species at 500 °C was examined using DRIFTS. Spectra from 0 min (which corresponds to when the reactant gas stream is ceased (i.e. reaction end)) to 10 min under Ar purging for the 3DOM LSMO, 1Pd/3DOM LSMO and 1AuPd/3DOM LSMO samples are shown in Figure S18. The strength by which the adsorbed species are attached to the catalyst differs significantly depending on the presence of Pd and Au-Pd. Most of the species do not bond strongly to the neat 3DOM LSMO, while the bonding strength when Pd is present increases substantially. After 10 min under the Ar flow, the intermediates remain on the Pd deposits, agreeing with other reports on the strong bonding strength of Pd.[50] However, the presence of Au weakens the bonding strength between the Pd and the intermediate species. According to the literature,[51-52] on adding copper or gold to an active metal like Pd, the Pd atoms are isolated and diluted in an Au–matrix (which behaves like supported, highly–dispersed Pd catalysts), leading to an electronic “ligand effect”. Thus, the strength of the bond between the reactant or intermediate molecule and the surface atoms can be modified by the electronic interaction between the surface atom and its neighbor. From our observations, we conclude that the Au has at least two different roles in our catalytic system: (1) to modify the electronic structure of the catalyst surface and (2) promote the presence of adsorbed oxygen species which, in turn, impact on the reaction mechanism. Firstly, the additional activated oxygen species on the Au and LSMO surfaces accelerates the reaction such that either the CH_3^- species are oxidized to CH_2O which then rapidly dissociates into HCOO– species or the CH_3^- species are oxidized directly into $HCOO^-$ species (explaining the lack of CH_2O species observed in the DRIFTS spectra). It has been reported that the electrophilicity of adsorbed oxygen can enhance the dissociation of CH_3^-.[53-54] Under the elevated activated oxygen environment, the $HCOO^-$ species also tend to be oxidized to carbonates rather than associate into CO_2. This corresponds to literature [41] reports whereby when the $O_2/CH_4 > 2$ adsorbed $HCOO^-$ species are prone to convert to carbonates. Secondly, the weaker species (e.g. CH_3^-) bond strength invoked by the Au–Pd alloy may improve intermediate mobility. This demonstrated by the spectra in Figure S18 where CH_3^- is desorbed rapidly under an Ar flow. That is, CH_3^- can move freely from Pd to Au and/or the LSMO surface where it can more readily interact with the additional O^- species which accelerates the oxidation reaction. Consequently, the weakened intermediate bonding strength invoked by the Au can also facilitate the oxidation process.

4. **CONCLUSION**

Bimetallic AuPd/3DOM LSMO catalysts with high surface areas (32.0–33.8 m^2/g) for methane oxidation were successfully fabricated. The bimetallic catalysts, possessing a unique 3DOM structure and Au-Pd alloy arrangement, gave excellent catalytic activity which was found to be a combined effect of both the support and Au-Pd NPs including (i) the high surface area, (ii) richness in adsorbed oxygen, (iii) oxidized noble metal species on the surface, (iv) modified electronic structure of the Au–Pd alloy, (v) low-temperature reducibility, and (vi) strong interaction between the Au–Pd alloy and the 3DOM support. The distinctive 3DOM structure, stable NP size and electron interaction within the bimetallic alloy allowed for optimized thermal and hydrothermal stability displayed by the AuPd/3DOM LSMO catalysts. *In-situ* DRIFTS investigations showed that including Au in the Au-Pd bimetallic system altered the reaction pathway and accelerated the reaction rate. The benefits were attributed to the Au weakening the bonding strength between the reaction intermediates and the Pd atoms and intensifying the adsorbed oxygen species on the surface of the catalyst.

ASSOCIATED CONTENT

Corresponding Authors

*E–mail for Dr. Hamidreza Arandiyan: h.arandiyan@unsw.edu.au; Tel.: +61-2-9385-7994

*E–mail for Dr. Jason Scott: jason.scott@unsw.edu.au; Tel.: +61-2-9385-7361

*E–mail for Prof. Hongxing Dai: hxdai@bjut.edu.cn; Tel.: +86-10-6739-6118

Notes

The authors declare no competing financial interest.

Supporting Information

Catalyst characterization procedures, synthesis and size distribution of the PMMA microspheres, preparation of zAu$_1$Pd$_2$/3DOM LSMO, catalytic activity measurement, XRD pattern of 1AuPd/3DOM LSMO, SEM images of PMMA microspheres, HRTEM/HRSEM images of 3DOM LSMO and 1AuPd/3DOM LSMO, HAADF-STEM images of 1AuPd/3DOM LSMO, XPS spectra of the samples, HRTEM/HRSEM images of 1Pd/3DOM LSMO sample after 9 h of on-stream 5.0 vol% water treatment at 380 °C, effects of H_2 and O_2 pretreatments at 300 °C for 2 h over 1Au$_x$Pd$_y$/1DDN LSMO. This material is available free of charge via the Internet at http://pubs.acs.org.

ACKNOWLEDGMENTS

Y. Wang thanks the University International Postgraduate Award (UIPA) from The University of New South Wales for financing her PhD scholarship. H. Arandiyan acknowledges financial support through the Vice Chancellor Research Fellowship (RG142406) from The University of New South Wales. H. Dai acknowledges the financial support from the National Science Foundation of China (21377008) and National High Technology Research and Development Program ("863" Program) of China (2015AA034603).

REFERENCES

(1) McCarty, J. G. *Nature* **2000**, 403, 35-36.

(2) Chen, J.; Shi, W.; Yang, S.; Arandiyan, H.; Li, J. *J. Phys. Chem. C* **2011**, 115, 17400-17408.

(3) Meshkani, F.; Rezaei, M.; Andache, M. *J. Ind. Eng. Chem.* **2014**, 20, 1251-1260.

(4) Chen, J.; Zhang, X.; Arandiyan, H.; Peng, Y.; Chang, H.; Li, J. *Catal. Today* **2013**, 201, 12-18.

(5) Chen, J.; Arandiyan, H.; Gao, X.; Li, J. *Catal. Surv. Asia* **2015**, 19, 140-171.

(6) Burroughs, M. C.; Bhaway, S. M.; Tangvijitsakul, P.; Cavicchi, K. A.; Soucek, M. D.; Vogt, B. D. *J. Phys. Chem. C* **2015**, 119, 12138-12148.

(7) Hutchings, G. J. *J. Catal.* **1985**, 96, 292-295.

(8) Hammer, B.; Norskov, J. K. *Nature* **1995**, 376, 238-240.

(9) Saiman, M. I.; Brett, G. L.; Tiruvalam, R.; Forde, M. M.; Sharples, K.; Thetford, A.; Jenkins, R. L.; Dimitratos, N.; Lopez-Sanchez, J. A.; Murphy, D. M.; Bethell, D.; Willock, D. J.; Taylor, S. H.; Knight, D. W.; Kiely, C. J.; Hutchings, G. J. *Angew. Chem. Int. Ed.* **2012**, 51, 5981-5985.

(10) Chen, M.; Kumar, D.; Yi, C.-W.; Goodman, D. W. *Science* **2005**, 310, 291-293.

(11) Levasseur, B.; Kaliaguine, S. *Appl. Catal., A* **2008**, 343, 29-38.

(12) Arandiyan, H.; Dai, H.; Deng, J.; Liu, Y.; Bai, B.; Wang, Y.; Li, X.; Xie, S.; Li, J. *J. Catal.* **2013**, 307, 327-339.

(13) Arandiyan, H.; Dai, H.; Deng, J.; Wang, Y.; Sun, H.; Xie, S.; Bai, B.; Liu, Y.; Ji, K.; Li, J. *J. Phys. Chem. C* **2014**, 118, 14913-14928.

(14) Arandiyan, H.; Dai, H.; Ji, K.; Sun, H.; Li, J. *ACS Catal.* **2015**, 5, 1781-1793.

(15) Arandiyan, H.; Scott, J.; Wang, Y.; Dai, H.; Sun, H.; Amal, R. *ACS Appl. Mater. Interfaces* **2016**, 8*,* 2457-2463.

(16) Xie, S.; Dai, H.; Deng, J.; Yang, H.; Han, W.; Arandiyan, H.; Guo, G. *J. Hazard. Mater.* **2014**, 279*,* 392-401.

(17) Liu, Y.; Dai, H.; Deng, J.; Li, X.; Wang, Y.; Arandiyan, H.; Xie, S.; Yang, H.; Guo, G. *J. Catal.* **2013**, 305*,* 146-153.

(18) Li, X.; Dai, H.; Deng, J.; Liu, Y.; Xie, S.; Zhao, Z.; Wang, Y.; Guo, G.; Arandiyan, H. *Chem. Eng. J.* **2013**, 228*,* 965-975.

(19) Xie, S.; Deng, J.; Zang, S.; Yang, H.; Guo, G.; Arandiyan, H.; Dai, H. *J. Catal.* **2015**, 322*,* 38-48.

(20) Arandiyan, H.; Dai, H.; Deng, J.; Wang, Y.; Xie, S.; Li, J. *Chemical Communications* **2013**, 49*,* 10748-10750.

(21) Yan, H.; Blanford, C. F.; Holland, B. T.; Smyrl, W. H.; Stein, A. *Chem. Mater.* **2000**, 12*,* 1134-1141.

(22) Wei, Y.; Liu, J.; Zhao, Z.; Duan, A.; Jiang, G.; Xu, C.; Gao, J.; He, H.; Wang, X. *Energy Environ. Sci.* **2011**, 4*,* 2959-2970.

(23) Tan, W.; Guo, G.; Deng, J.; Xie, S.; Yang, H.; Jiang, Y.; Dai, H. *Ind. Eng. Chem. Res.* **2014**, 53*,* 18452-18461.

(24) Xie, S.; Deng, J.; Liu, Y.; Zhang, Z.; Yang, H.; Jiang, Y.; Arandiyan, H.; Dai, H.; Au, C. T. *Appl. Catal., A* **2015**, 507*,* 82-90.

(25) Kesavan, L.; Tiruvalam, R.; Rahim, M. H. A.; bin Saiman, M. I.; Enache, D. I.; Jenkins, R. L.; Dimitratos, N.; Lopez-Sanchez, J. A.; Taylor, S. H.; Knight, D. W.; Kiely, C. J.; Hutchings, G. J. *Science* **2011**, 331*,* 195-199.

(26) Long, J.; Liu, H.; Wu, S.; Liao, S.; Li, Y. *ACS Catal.* **2013**, 3*,* 647-654.

(27) Liu, Y.; Dai, H.; Deng, J.; Xie, S.; Yang, H.; Tan, W.; Han, W.; Jiang, Y.; Guo, G. *J. Catal.* **2014**, 309*,* 408-418.

(28) Rousseau, S.; Loridant, S.; Delichere, P.; Boreave, A.; Deloume, J. P.; Vernoux, P. *Appl. Catal., B* **2009**, 88*,* 438-447.

(29) Burch, R.; Crittle, D. J.; Hayes, M. J. *Catal. Today* **1999**, 47*,* 229-234.

(30) Fierro, J. L. G.; Tascón, J. M. D.; Tejuca, L. G. *J. Catal.* **1984**, 89*,* 209-216.

(31) Rodríguez-González, L.; Hermes, F.; Bertmer, M.; Rodríguez-Castellón, E.; Jiménez-López, A.; Simon, U. *Appl. Catal., A* **2007**, 328*,* 174-182.

(32) Fu, W.; Li, X.-H.; Bao, H.-L.; Wang, K.-X.; Wei, X.; Cai, Y.-Y.; Chen, J.-S. *Sci. Rep.* **2013**, 3*,* 2349.

(33) Cullis, C. F.; Willatt, B. M. *J. Catal.* **1983**, 83*,* 267-285.

(34) Burch, R.; Urbano, F. J. *Appl. Catal., A* **1995**, 124*,* 121-138.

(35) Farrauto, R. J.; Hobson, M. C.; Kennelly, T.; Waterman, E. M. *Appl. Catal., A* **1992**, 81*,* 227-237.

(36) Matam, S. K.; Aguirre, M. H.; Weidenkaff, A.; Ferri, D. *J. Phys. Chem. C* **2010**, 114*,* 9439-9443.

(37) Wang, C.-H.; Chen, C.-L.; Weng, H.-S. *Chemosphere* **2004**, 57*,* 1131-1138.

(38) Ferrari, A. M.; Huber, S.; Knözinger, H.; Neyman, K. M.; Rösch, N. *J. Phys. Chem. B* **1998**, 102*,* 4548-4555.

(39) Elmasides, C.; Kondarides, D. I.; Grünert, W.; Verykios, X. E. *J. Phys. Chem. B* **1999**, 103*,* 5227-5239.

(40) Schmal, M.; Souza, M. M. V. M.; Alegre, V. V.; da Silva, M. A. P.; César, D. V.; Perez, C. A. C. *Catal. Today* **2006**, 118*,* 392-401.

(41) Li, Z.; Xu, G.; Hoflund, G. B. *Fuel Process. Technol.* **2003**, 84*,* 1-11.

(42) Li, C.; Domen, K.; Maruya, K. I.; Onishi, T. *J. Chem. Soc., Chem. Commun.* **1988**, 1541-1542.

(43) Raskó, J.; Kiss, J. *Catal. Lett.* 111*,* 87-95.

(44) Liao, L.-F.; Wu, W.-C.; Chen, C.-Y.; Lin, J.-L. *J. Phys. Chem. B* **2001**, 105*,* 7678-7685.

(45) Chuang, C.-C.; Wu, W.-C.; Huang, M.-C.; Huang, I. C.; Lin, J.-L. *J. Catal.* **1999**, 185*,* 423-434.

(46) Burch, R.; Hayes, M. J. *J. Mol. Catal. A: Chem.* **1995**, 100*,* 13-33.

(47) Fujimoto, K.-i.; Ribeiro, F. H.; Avalos-Borja, M.; Iglesia, E. *J. Catal.* **1998**, 179*,* 431-442.

(48) Xu, J.; Ouyang, L.; Mao, W.; Yang, X.-J.; Xu, X.-C.; Su, J.-J.; Zhuang, T.-Z.; Li, H.; Han, Y.-F. *ACS Catal.* **2012**, 2*,* 261-269.

(49) Chin, Y.-H.; Buda, C.; Neurock, M.; Iglesia, E. *J. Am. Chem. Soc.* **2013**, 135*,* 15425-15442.

(50) Zhao, Z.-J.; Chiu, C.-c.; Gong, J. *Chem. Sci.* **2015**, 6*,* 4403-4425.

(51) Burch, R. *Acc. Chem. Res.* **1982**, 15*,* 24-31.

(52) Liu, P.; Norskov, J. K. *PCCP* **2001**, 3*,* 3814-3818.

(53) Silva, I. C. d.; Appel, L. G.; Braun, S. *Appl. Catal., A* **2006**, 314*,* 172-178.

(54) Nasser, H.; Rédey, Á.; Yuzhakova, T.; Kovács, J. *React. Kinet. Catal. Lett.* **2008**, 94*,* 165-173.

Table 1. Macropore diameters, BET surface areas, crystallite sizes (D_{support}), pore volumes, noble metal particle sizes, and actual AuPd loadings of the samples.

Sample	Macropore diameter[a] (nm)	BET surface area (m^2/g)	Pore volume (cm^3/g)	D_{support}[b] (nm)	Mean metal particle size[c] (nm)	Au content[d] (wt%)	Pd content[d] (wt%)	Noble metal loading[d]	
								Nominal (wt%)	Measured (wt%)
3DOM LSMO	140-153	32.4	0.123	36	-	-	-	-	-
1Au/3DOM LSMO	130-145	32.6	0.119	34	2.4	0.94	-	1	0.94
1Pd/3DOM LSMO	135-150	32.0	0.130	35	2.3	-	0.85	1	0.85
1AuPd/3DOM LSMO	126-138	33.6	0.106	34	2.2	0.44	0.48	1	0.92
2AuPd/3DOM LSMO	130-140	33.3	0.114	35	2.0	0.95	0.98	2	1.93
3AuPd/3DOM LSMO	128-135	33.8	0.113	35	2.2	1.42	1.50	3	2.92
1AuPd/1DDN LSMO	-	4.32	0.017	55	2.1	0.45	0.50	1	0.95

[a] Data were estimated according to the SEM images.
[b] Calculated based on the XRD results according to Scherrer's equation.
[c] Estimated by statistical analysis of more than 200 NPs in TEM images.
[d] Determined using ICP-AES analysis.

Table 2. The specific reaction rates, turnover frequencies (TOFs) and activation energies (E_a) of the 3DOM LSMO, AuPd/3DOM LSMO, and 1AuPd/1DDN LSMO samples.

	Methane oxidation at 270°C		Specific reaction rate at 270°C			Kinetic parameter
Sample	$TOF_{Au\text{-}Pd}$ ($\times 10^{-3}$ s^{-1})	TOF_{cat} ($\times 10^{-3}$ s^{-1})	μmol/(g_{cat} s)	μmol/($g_{Au\text{-}Pd}$ s)	μmol/(g_{LSMO} s)	E_a (kJ/mol)
3DOM LSMO	-	0.08	0.38	-	0.38	92.8
1Au/3DOM LSMO	9.45	0.11	0.77	76.8	0.78	76.1
1Pd/3DOM LSMO	11.2	0.21	0.93	92.8	0.94	72.2
1AuPd/3DOM LSMO	13.5	0.22	0.99	99.2	1.00	56.4
2AuPd/3DOM LSMO	15.3	0.51	2.24	112	2.29	50.5
3AuPd/3DOM LSMO	16.0	0.80	3.52	117	3.63	46.3
1AuPd/1DDN LSMO	10.2	0.20	0.90	89.5	0.90	72.4

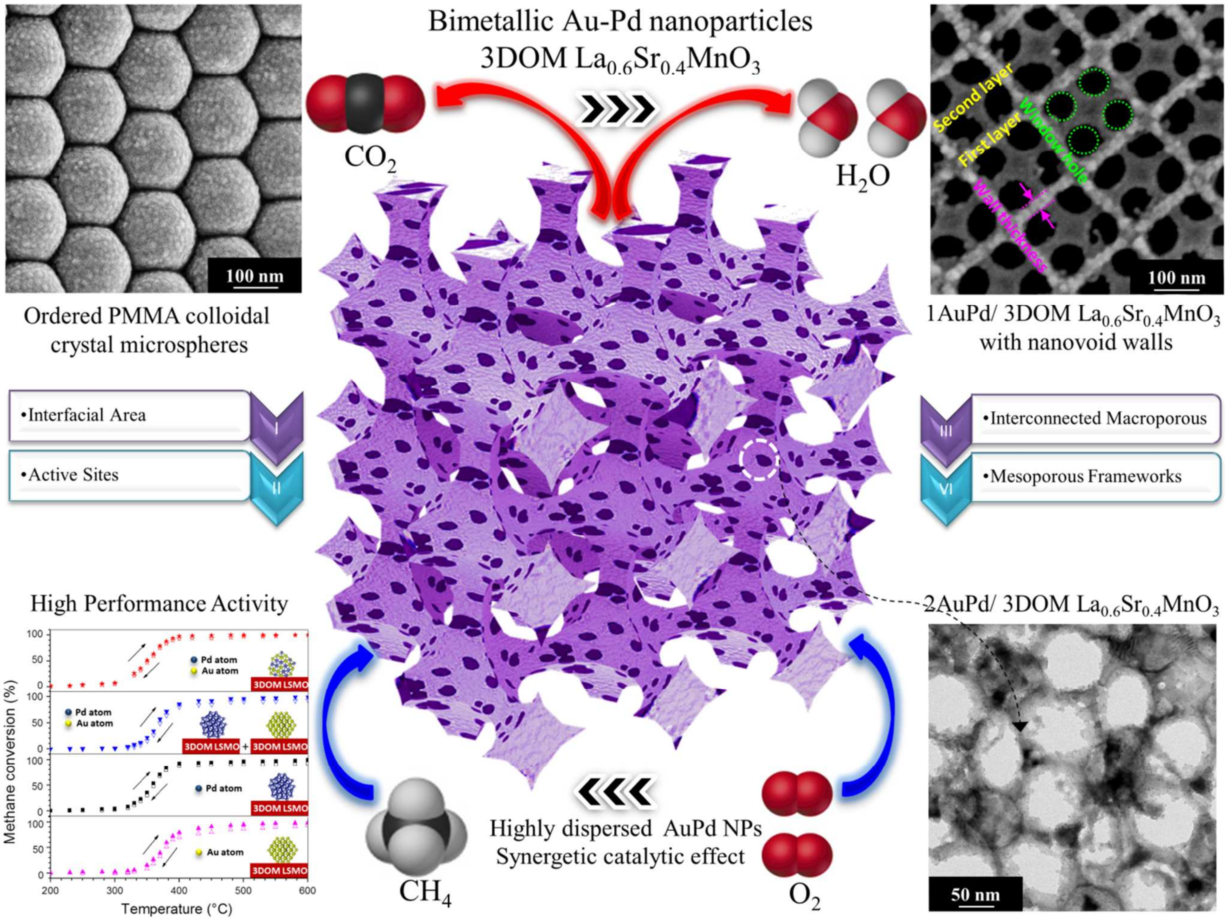

Scheme 1. Schematic illustration of the AuPd/3DOM LSMO catalyst.

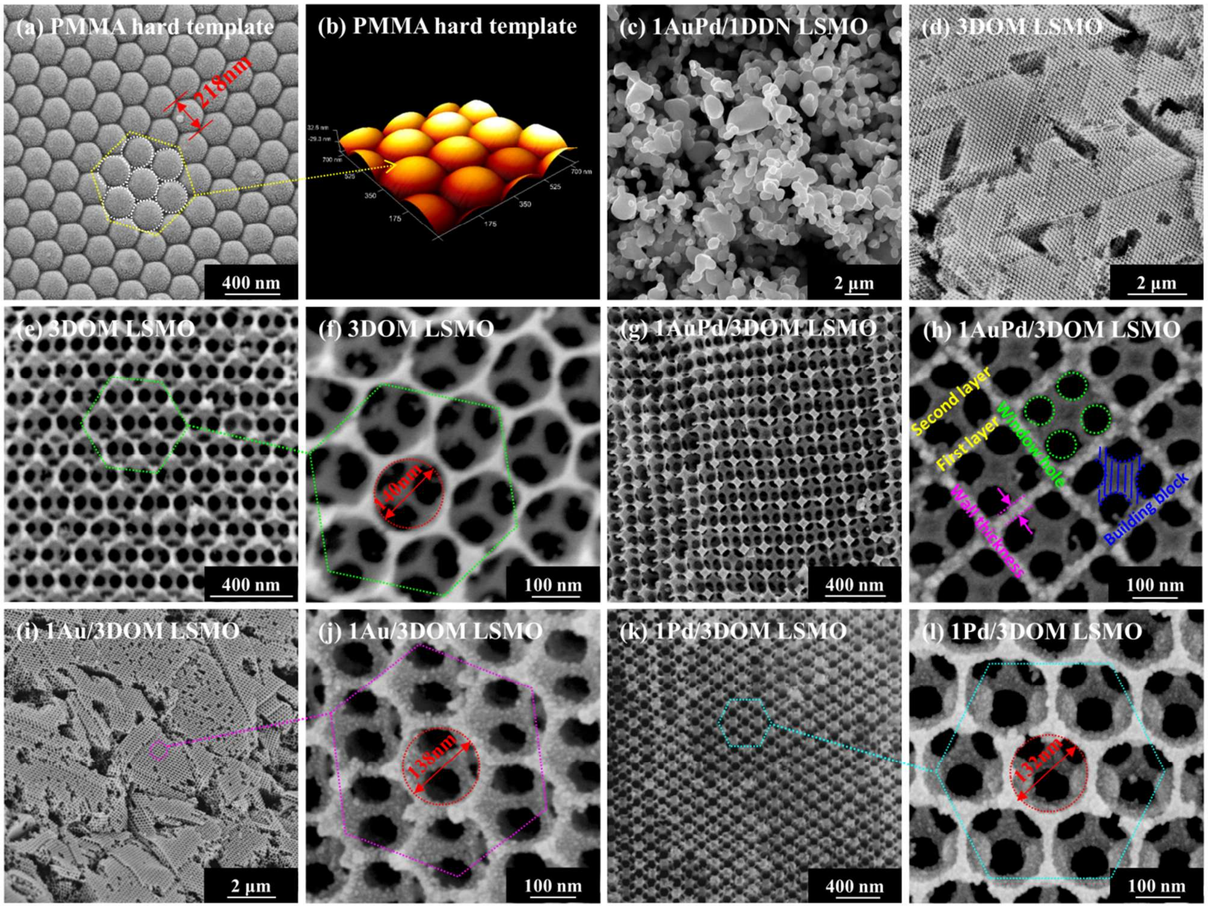

Figure 1. HRSEM and 3D-eAFM images of PMMA, 3DOM LSMO, noble metal supported 3DOM LSMO and 1DDN LSMO.

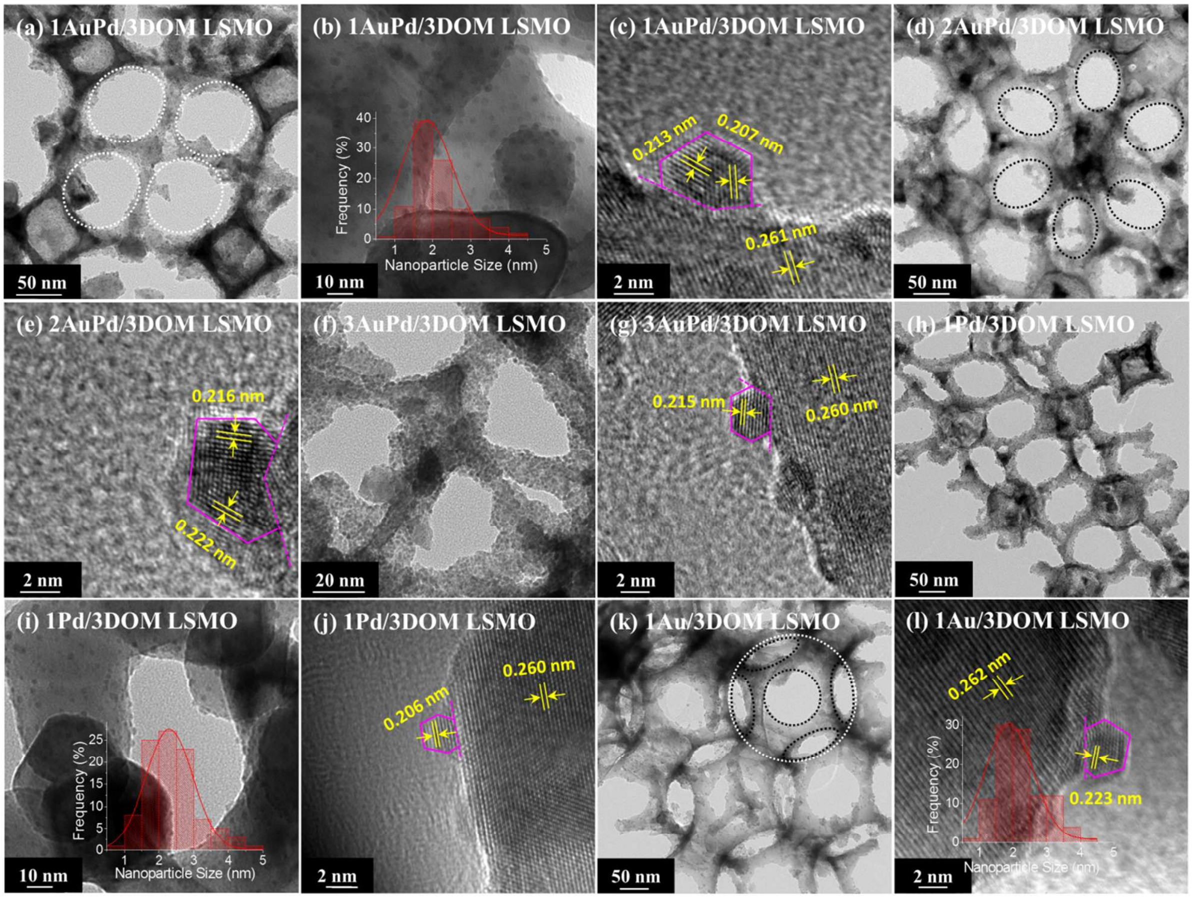

Figure 2. HRTEM images of monometallic Au and Pd and bimetallic AuPd/3DOM LSMO catalysts.

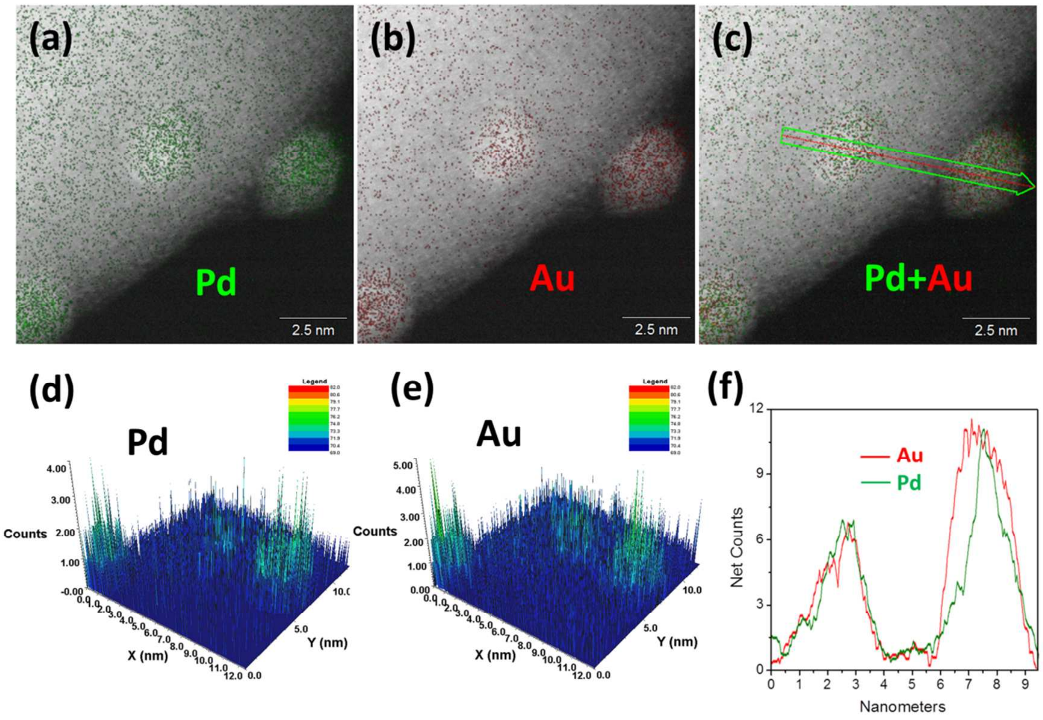

Figure 3. HAADF-STEM images and EDS elemental maps for 1AuPd/3DOM LSMO sample of (a-c) EDS elemental maps of Pd, Au and combined of Au+Pd, (d, e) 3D visualization of Pd and Au and (f) EDS intensity line profiles extracted from the spectrum image along the line drawn on image (c).

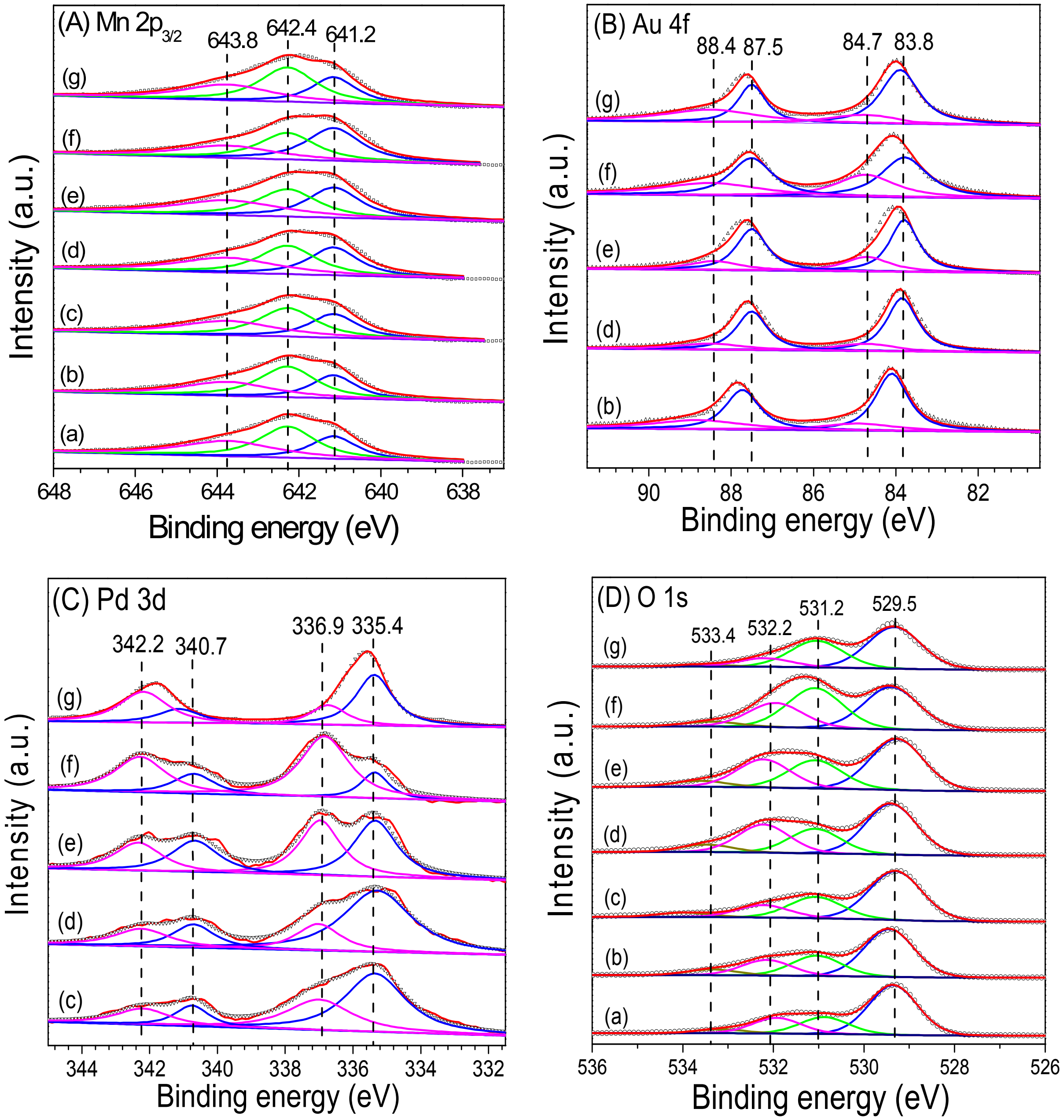

Figure 4. (A) Mn $2p_{3/2}$, (B) Au 4f, (C) Pd 3d, and (D) O 1s XPS spectra of (a) 3DOM LSMO, (b) 1Au/3DOM LSMO, (c) 1Pd/3DOM LSMO, (d) 1AuPd/3DOM LSMO, (e) 2AuPd/3DOM LSMO, (f) 3AuPd/3DOM LSMO and (g) 1AuPd/1DDN LSMO.

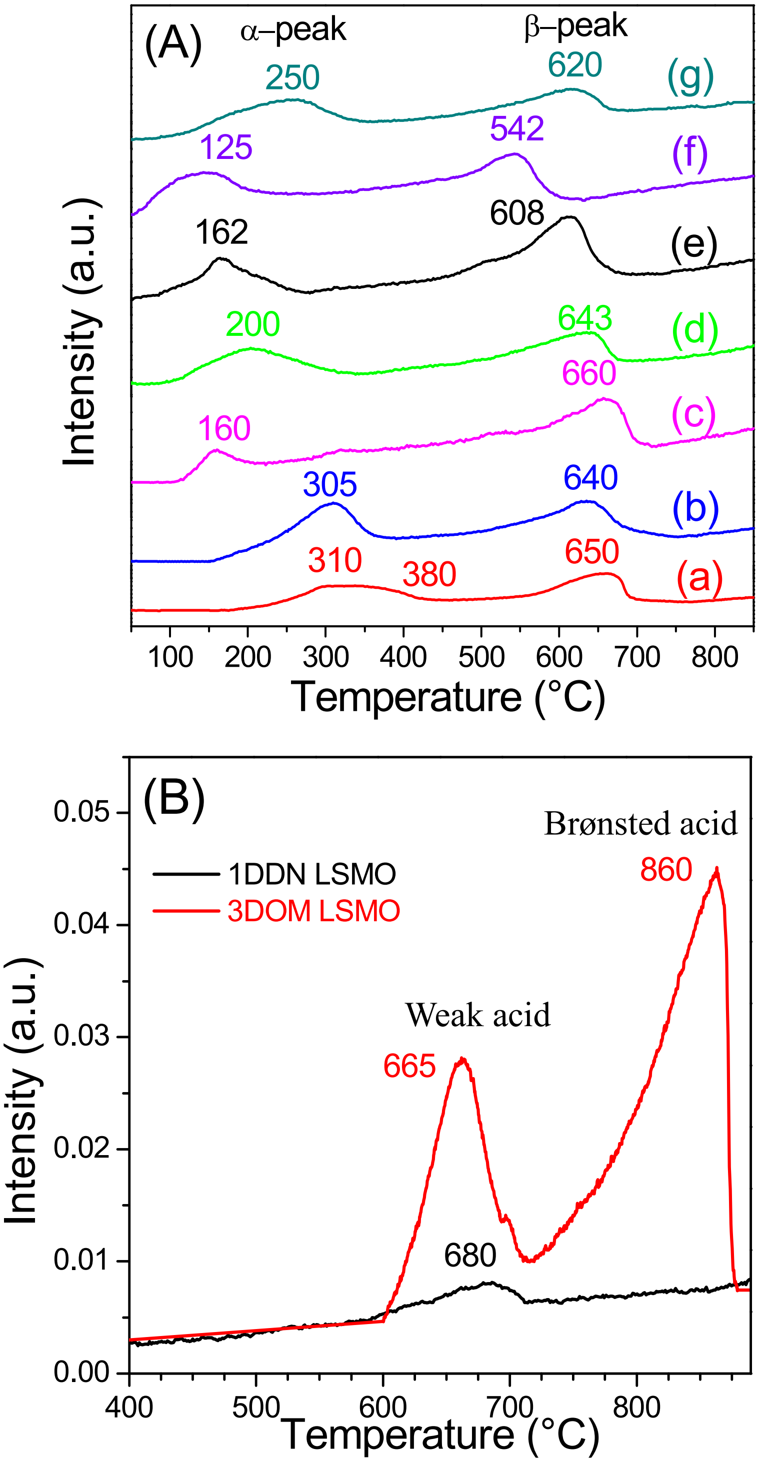

Figure 5. (A) H_2-TPR profiles of (a) 3DOM LSMO, (b) 1Au/3DOM LSMO, (c) 1Pd/3DOM LSMO, (d) 1AuPd/3DOM LSMO, (e) 2AuPd/3DOM LSMO, (f) 3AuPd/3DOM LSMO and (g) 1AuPd/1DDN LSMO; and (B) NH_3-TPD profiles of 1DDN LSMO and 3DOM LSMO samples.

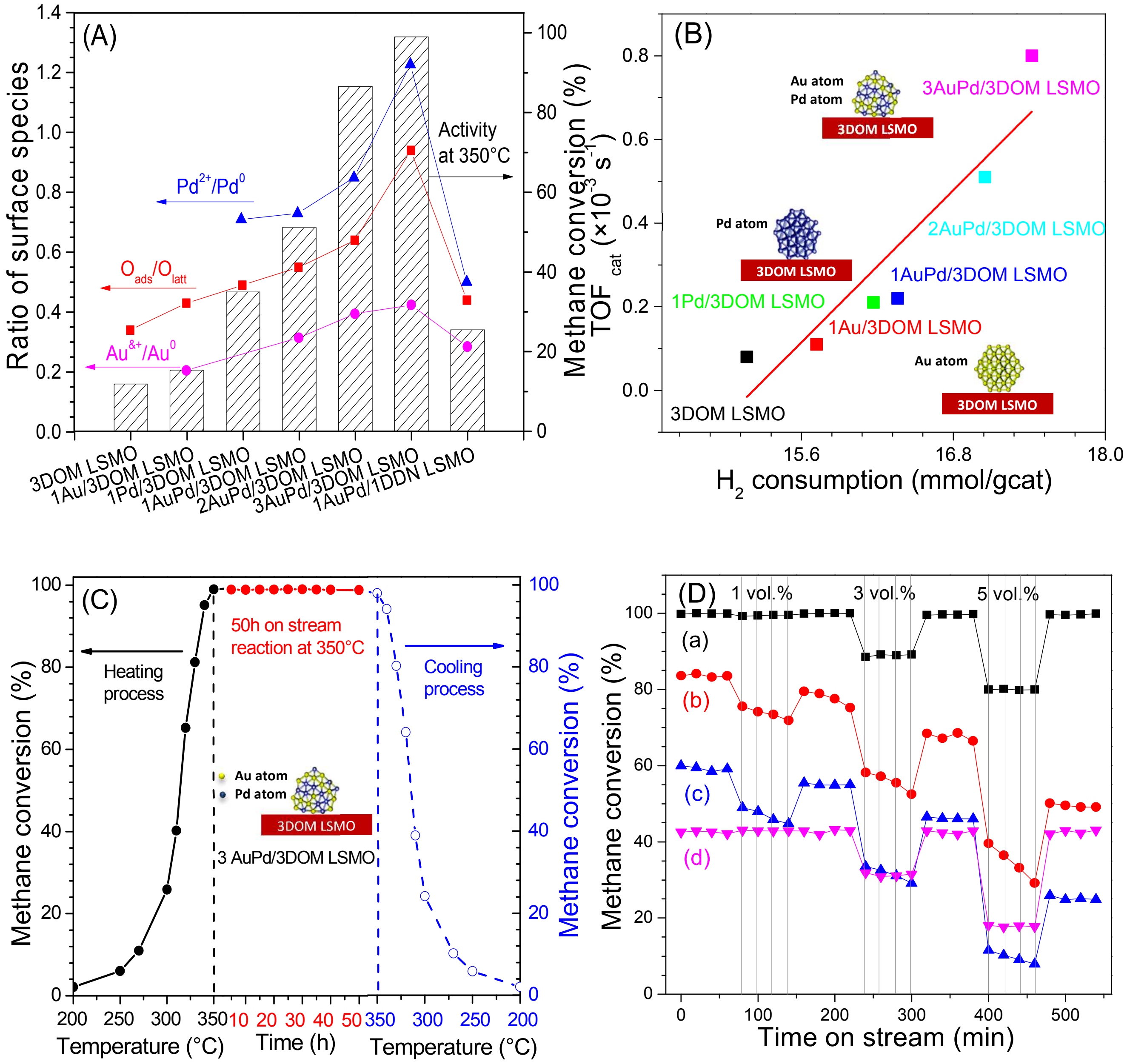

Figure 6. (A) Dependence of methane conversion at 350 °C and ratio of O_{ads}/O_{latt}, Pd^{2+}/Pd^0 and $Au^{\delta+}/Au^0$, (B) correlation of the TOF at 270 °C and the H_2 consumption over the obtained samples, (C) methane conversion over 3AuPd/3DOM LSMO at 350 °C within 50 h of on-stream reaction and (D) effect of water vapor concentration at 380 °C on the activity for methane combustion over (a) 3AuPd/3DOM LSMO, (b) 1Pd/3DOM LSMO, (c) 1Au/3DOM LSMO and (d) 3DOM LSMO (The striped areas show when water vapor was added).

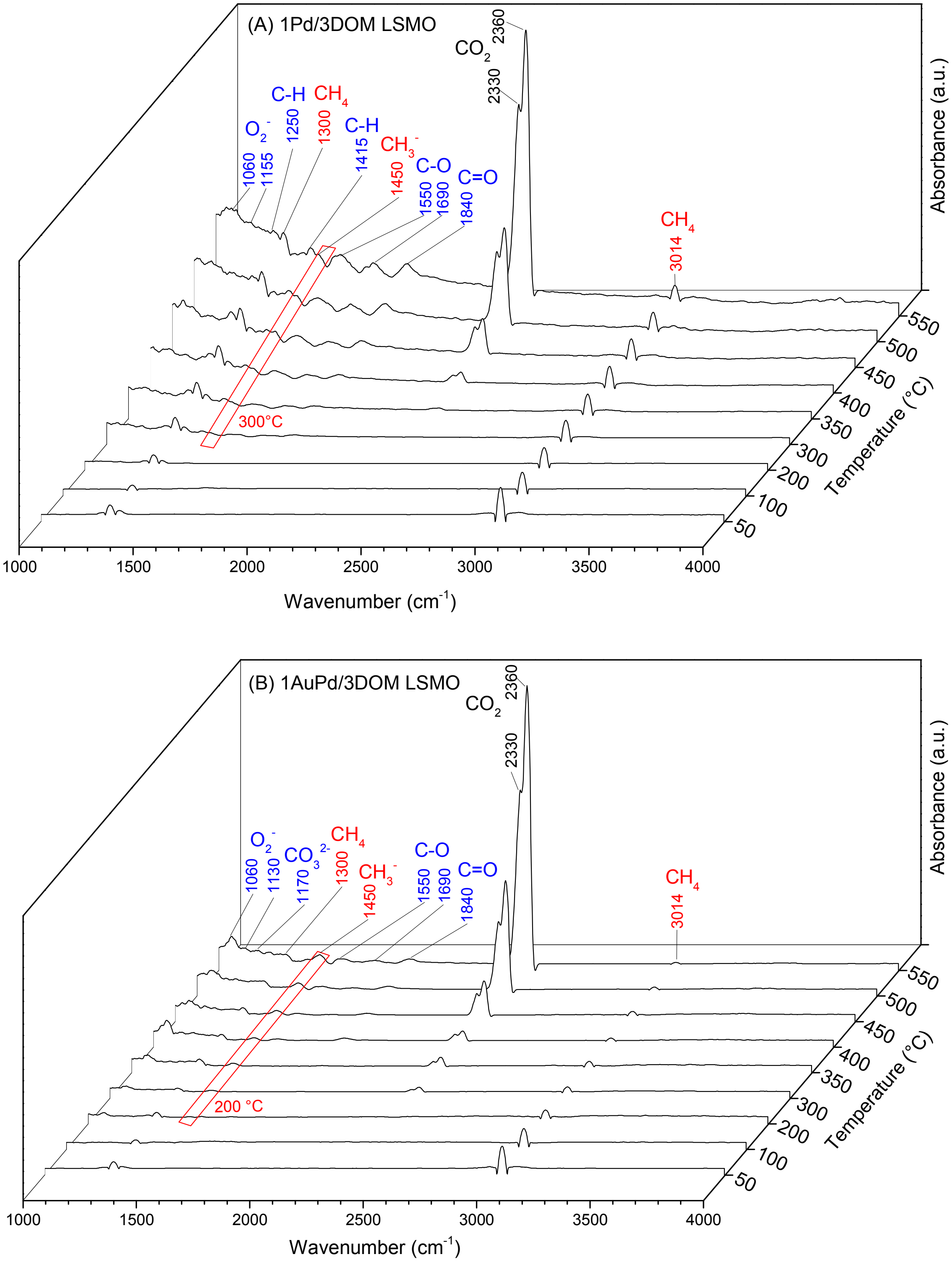

Figure 7. In situ DRIFT spectra of methane oxidation over (A) 1Pd/3DOM LSMO and (B) 1AuPd/3DOM LSMO.

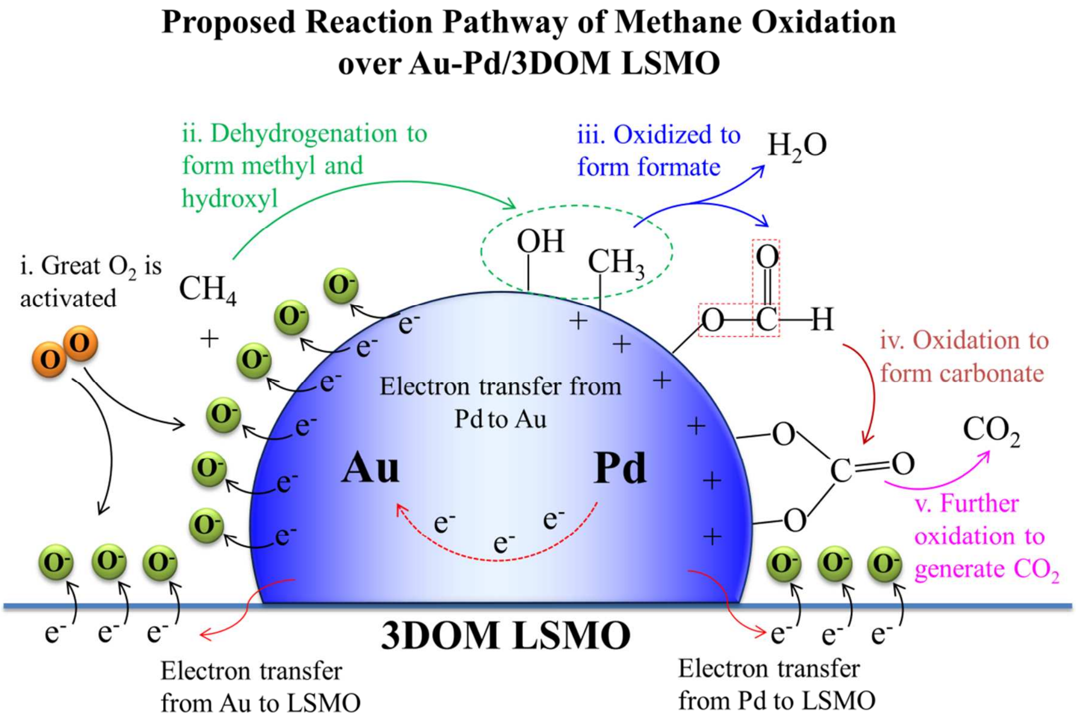

Scheme 2. Proposed elementary steps for the oxidation of methane over 1AuPd/3DOM LSMO.

TOC Graphic

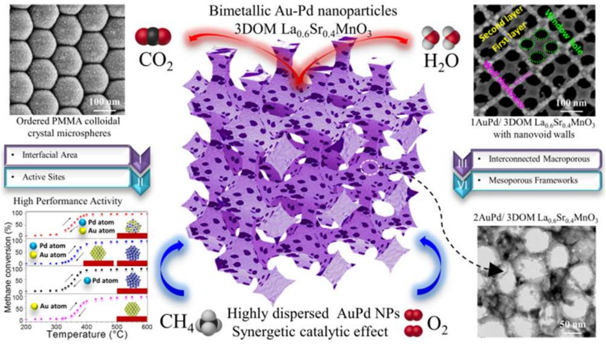
Bimetallic Au-Pd nanoparticles
3DOM $La_{0.6}Sr_{0.4}MnO_3$
CO_2
H_2O
100 nm
Ordered PMMA colloidal crystal microspheres
Second layer
First layer
Window hole
100 nm
1AuPd/ 3DOM $La_{0.6}Sr_{0.4}MnO_3$ with nanovoid walls
• Interfacial Area
I
• Active Sites
II
III
• Interconnected Macroporous
VI
• Mesoporous Frameworks
High Performance Activity
Methane conversion (%)
Temperature (°C)
200
300
400
500
600
0
50
100
Pd atom
Au atom
2AuPd/ 3DOM $La_{0.6}Sr_{0.4}MnO_3$
50 nm
CH_4
Highly dispersed AuPd NPs
Synergetic catalytic effect
O_2

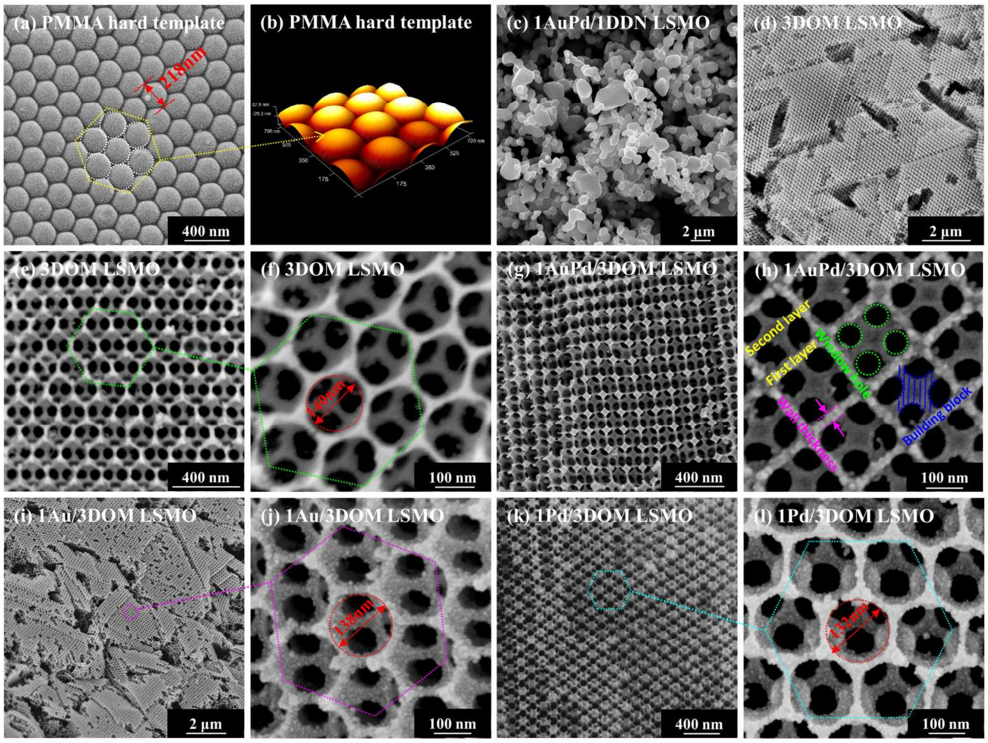

Figure 1-Revised High Resolution

190x142mm (300 x 300 DPI)

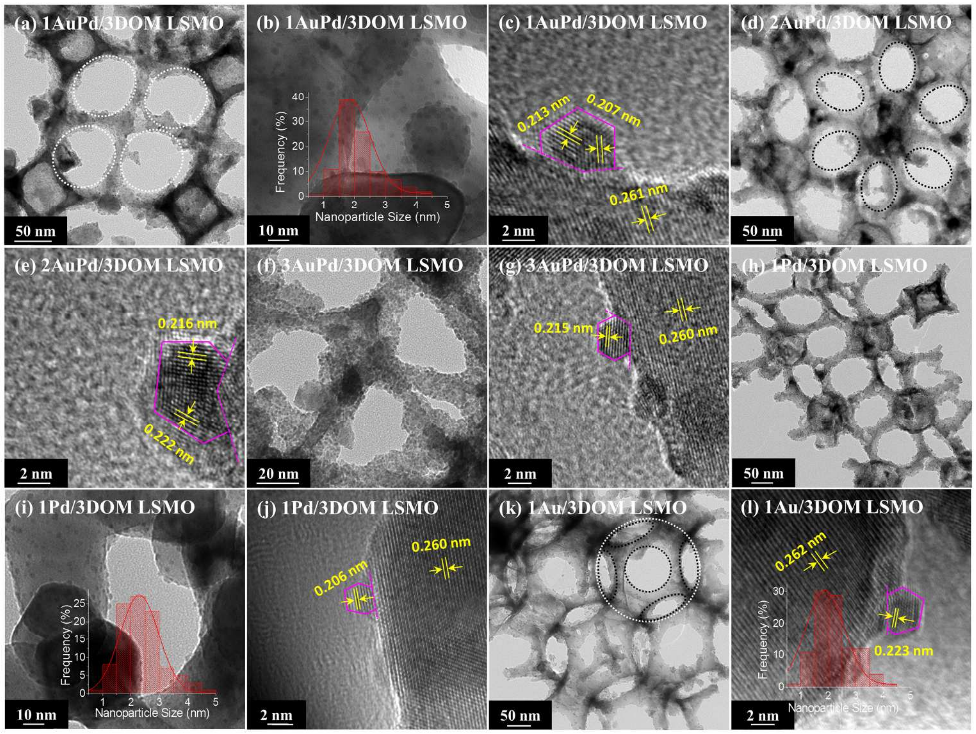

Figure 2-Revised High Resolution

190x142mm (300 x 300 DPI)

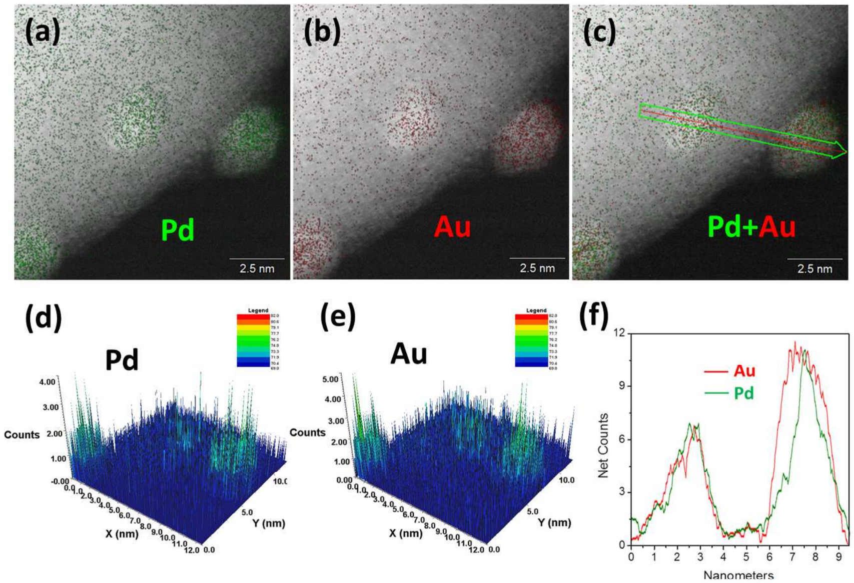

Figure 3-Revised High Resolution

190x142mm (300 x 300 DPI)

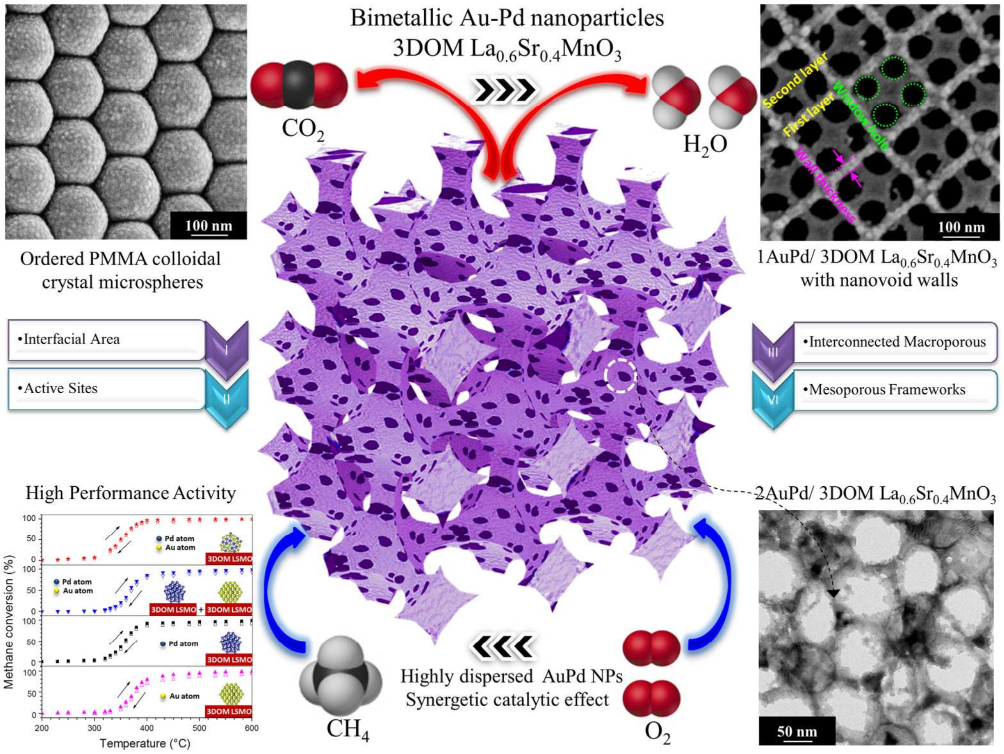

Scheme 1-Revised High Resolution

190x142mm (300 x 300 DPI)

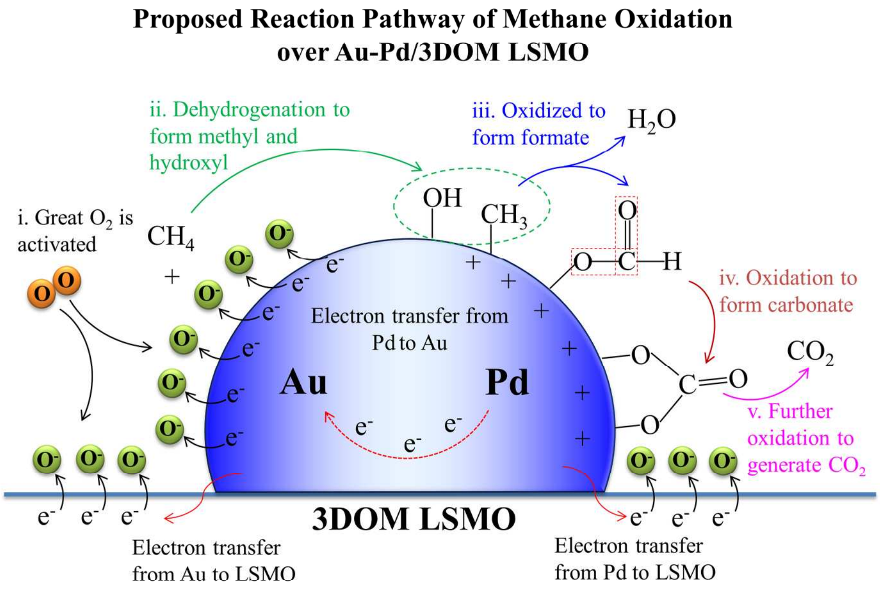

Scheme 2-Revised High Resolution

190x142mm (300 x 300 DPI)

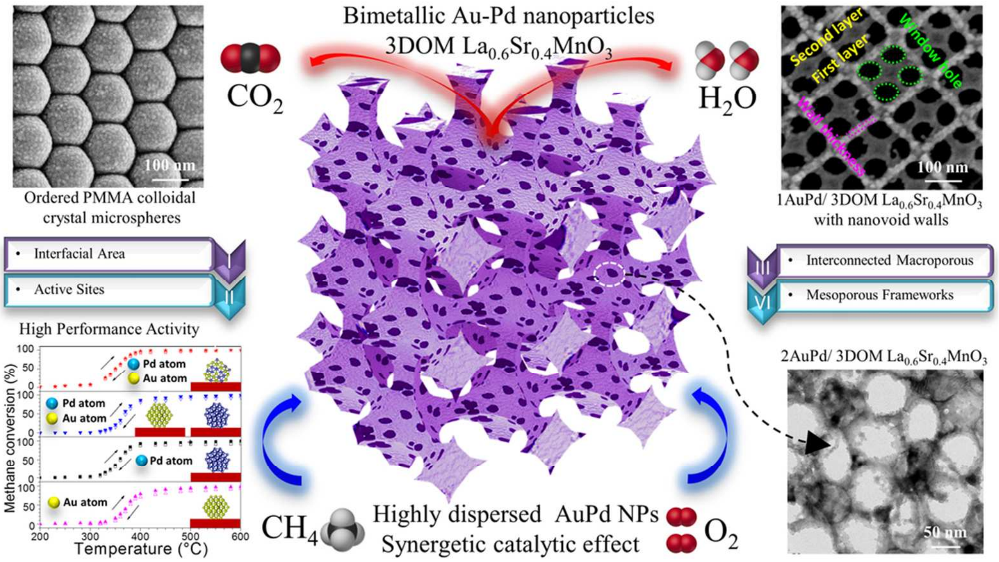

TOC-Revised High Resolution

47x26mm (600 x 600 DPI)